GALAXY CLUSTERS:
X-RAY CONTRIBUTIONS TO MULTI-WAVELENGTH CLUSTER STUDIES IN THE ERA OF MASS SENSITIVE CLUSTER SURVEYS.

By

AMRUTA J. DESHPANDE

A dissertation submitted to the

Graduate School—New Brunswick

Rutgers, The State University of New Jersey

in partial fulfillment of the requirements

for the degree of

Doctor of Philosophy

Graduate Program in Physics and Astronomy

written under the direction of

John P. Hughes

and approved by

New Brunswick, New Jersey

October, 2016

ABSTRACT OF THE DISSERTATION

Galaxy Clusters:

X-ray contributions to multi-wavelength cluster studies in the era of mass sensitive cluster surveys.

By AMRUTA J. DESHPANDE

Dissertation Director:

John P. Hughes

I present studies of the X-ray emission from galaxy clusters in the context of understanding the multi-wavelength selection function and mass estimation of galaxy clusters. Clusters are gravitationally bound systems of dark matter, gas and galaxies, and are the largest gravitationally bound structures in the Universe. Constraining cosmology with cluster studies requires large, complete cluster samples with reliable masses over cosmologically significant survey volumes. Such samples are only just becoming available with new surveying telescopes that have optimal sensitivity for cluster finding, and some with the additionally useful property of finding clusters largely by their mass, which is the cosmologically significant cluster property. These surveys have increased the need for obtaining large, well-understood samples of clusters for characterizing their selection. Ongoing work in this field aims to determine

the selection and limitations of the four ways of observing clusters and measuring their masses (optical/infrared, X-ray, weak lensing, or Sunyaev-Zel'dovich effect) using both large and small samples. In this context, I have studied small cluster samples in the X-ray and compared their properties to those determined through three different cluster selection methods: through weak lensing selection, optical selection, and selection through the Sunyaev-Zel'dovich effect. In this thesis I begin in the introduction with a brief overview of the current cosmological picture and how clusters help to constrain cosmology. In the subsequent chapters I describe my work in the X-ray, aimed at better understanding clusters selected through the different methods. I conclude with a summary of how my follow-up and other multi-wavelength studies have illuminated cluster selection and also with comments on the persisting need for similar studies in the near future.

Acknowledgments

I am tremendously grateful for the continued support of my advisor, Jack Hughes, my thesis committee which additionally includes Ted Williams, Saurabh Jha and , and Sang-wook Cheong, and the Rutgers faculty, without the support of whom I could not have successfully completed this degree. A special thank you to those faculty members, of which there are many, that take special care to inspire students. I would especially like to acknowledge the open environment fostered by the astronomy faculty that aims to involve graduate students at all levels of scientific discussion, from social to highly critical, and in this way to help students to develop professionally.

I am grateful to my parents for their trust and support, and to my sister for her unwavering cheer-leadership. I would like to acknowledge my grandmother whose openness, honesty, and spirit have always been an inspiration; she is dearly missed. Finally, I would be remiss to not acknowledge the student and post-doctoral body that has been just as helpful in both my scientific and personal growth: the first-year and second-year student body during my first year here, and since then a special note is due to Amit, Jade, Lisa, George, Mike, Luke, Mrinal, Vivi, and Jean.

Dedication

For scientific pursuits of Truth.

For AST.

For Shalini,

Jayant,

Nilima,

and

Madhura.

Table of Contents

Abstract ii

Acknowledgments iv

Dedication v

List of Tables ix

List of Figures x

1. Introduction 1

1.1. The Formation of the Universe 1

1.2. The Expanding Universe 2

1.3. Framework for Cosmological Models 4

1.4. Distance Measures 6

1.5. Hierarchical Structure Formation 7

1.6. Clusters 8

1.6.1. Cluster galaxies 8

1.6.2. Cluster gas (the Intra-Cluster Medium) 9

1.6.3. Cluster dark matter 10

1.7. Cluster Detection 12

1.7.1. Optical 12

1.7.2. X-ray 14

1.7.3. Weak Lensing 16

1.7.4. Sunyaev-Zel'dovich Effect 18

1.8. Cluster Mass Determination 21

1.8.1. Optical 21

1.8.2. X-ray 23

1.8.3. Weak Lensing 24

1.9. Cosmology from clusters 25

1.9.1. Cluster counts: $dN/dM/dz$. 25

1.9.2. Cluster gas mass fraction: f_{gas} 26

1.10. X-ray Analysis 26

1.10.1. *XMM Newton* 27

1.10.2. X-ray backgrounds 28

2. A Weak lensing Selected Cluster Sample 29

2.1. Introduction 29

2.2. The Sample, X-ray Data, & Analysis 31

2.2.1. Imaging 32

2.2.2. Source Detection 33

2.2.3. Extracting Spectra 39

2.2.4. Measure X-ray Temperature & Luminosity 40

2.2.5. The resulting L_X, T_X of sample. 48

2.2.6. The $L_X - T_X$ relation 49

2.3. Mass Estimates & Comparison 50

2.3.1. X$-$ray Mass Estimates 51

2.3.2. Weak Lensing Mass Estimates 53

2.3.3. X-ray $-$ Weak Lensing Mass Comparison 54

2.4. Summary 59

3. X-ray properties of SZE selected clusters from the ACT 2008 observing season. 62

3.1. Introduction 62

3.2. Data Analysis 63

3.3. Results 66

3.4. Discussion 68

4. Follow-up of optically selected clusters as a comparison sample for ACT. 70

4.1. Introduction 70

4.2. *XMM Newton* follow-up 71

4.3. Discussion 75

Conclusion 77

Bibliography 82

List of Tables

2.1. *XMM-Newton* observations. 31

2.2. X-ray clusters in the *XMM Newton* observations of DLS shear peaks. 34

2.3. *XMM Newton* spectral fitting results: temperature and luminosity . . 38

2.4. R_{500}, T_{500}, & M_{500} 53

3.1. *XMM Newton* Cluster Properties 65

4.1. Optical Clusters Located within the Field of View of XMM-Newton Observations 73

List of Figures

1.1. Schematic of weak lensing effect. 17

1.2. Schematic of shifted spectrum due to the SZE. 18

2.1. Subdivision of shear-selected clusters by X-ray properties. 33

2.2. Images of shear-selected clusters with significant X-ray emission. . . . 36

2.3. DLSCL J0522.2-4820 X-ray images and spectra. 42

2.4. DLSCL J0916.0+2931 X-ray images and spectra. 43

2.5. DLSCL J1055.2-0503 X-ray images and spectra. 44

2.6. DLSCL J1048.5-0411 X-ray images and spectra. 45

2.7. DLSCL J0916.3+3025 X-ray image. 46

2.8. L_X-T_X relation for shear-selected clusters. 47

2.9. Comparison of X-ray masses from two scaling laws. 52

2.10. X-ray to weak lensing mass comparison. 55

2.11. Weak lensing and X-ray mass comparison for different choices of cluster radii. 59

3.1. X-ray images of ACT clusters at low, medium, and high redshift. . . . 64

Chapter 1

Introduction

1.1 The Formation of the Universe

Under the current paradigm of the Big Bang Theory, the Universe is believed to have begun 13.8 billion years ago (e.g., Planck Collaboration et al. 2015) and has been expanding ever since. Primordial fluctuations to an initially smooth mass density field established in the early universe are said to be the seeds of the structure we see today. Structure here, and throughout this thesis, refers to organized matter (e.g., stars, galaxies, clusters voids, etc.). Matter in the early Universe is described as a quark-gluon plasma that interacts primarily through the strong and weak forces. This hot and very dense state is due to the small physical size of the Universe, which is a closed system and must have then contained all of the matter that we see in the Universe today. From this state, the Universe continued to expand and also cooled adiabatically, making more relevant the laws (e.g., the electromagnetic force) that we see governing the much cooler universe today. The basic building blocks of matter formed when the electromagnetic force became important and the baryons, leptons and photons were coupled. In this environment, Big Bang Nucleosynthesis describes these particle interactions, balancing particle creation and annihilation rates and explains the formations of hydrogen (75%), helium (25%), and lithium (trace amounts) in the early Universe.

At a redshift of $z \sim 1100$, photons decouple from matter and begin to stream freely. There are a few things to note about this epoch. First, this is the farthest back into the Universe from when we can receive light. The free-streaming radiation released at this time, the cosmic microwave background (CMB) radiation, is a relic that is still observable today at longer wavelengths and is said to come from the surface of last scattering. The wavelengths of the CMB have expanded with the Universe to the microwave regime today and the radiation is fit well with a black body spectrum (e.g., Planck Collaboration et al. 2015). There are millions of CMB photons per cubic meter, and they contain imprints from their former coupled life with the baryonic matter. One such imprint is produced by the Baryon Acoustic Oscillations (BAO), which are harmonic (spatial) density waves (sound) at the causal distance scale of the surface of last scattering. Acoustic density peaks produce small distortions in the CMB at the causal spatial scale, which are otherwise also observable as enhancements in the correlation of large scale structure at the same scale.

The large scale structure of the Universe also leaves an imprint on the CMB. Primordial density fluctuations distort the CMB temperature within their bounds to one part in a hundred thousand. Density fluctuations are dominated by dark matter which outweighs baryonic matter by $5:1$. Baryons, here, is astronomical terminology for baryonic and leptonic matter that interacts electromagnetically. Dark matter, in contrast, only interacts gravitationally and is further specified to be non-relativistic (or cold) so as to preserve (not wash out) the density perturbations that have left a measured imprint on the CMB.

1.2 The Expanding Universe

Hubble (1929) showed that galaxies in the local Universe are receding away from us with velocities that scale linearly (as H_0, the Hubble parameter) with their distance from us as $v = H_0 d$, a claim that has since been well confirmed (e.g., Riess et al. 1996). This expansion complicates distance determination as local distance rulers cannot be applied to objects much farther away. Typically, galaxy velocities are easier to measure as they can be obtained from the observed, Doppler-shifted values of known emission lines of galaxies. The redshift, $z = \frac{\Delta\lambda}{\lambda_{emitted}}$, also relates simply to the receding velocity for small values of velocity compared to the speed of light, which is the case for astronomical measurements, as $v = cz$. And so, this relation combined with Hubble's velocity-distance relation, or the Hubble Law, relates redshift directly to distance as $cz = H_0 d$ (in the local Universe). Generally, the redshift is used as a practical indicator of how far away something is from us.

Two concepts that are useful to define in dealing with the expanding Universe are the scale factor and the comoving distance. The scale factor is a factor by which the Universe has expanded, normalized to distance measurements today. It thus equals one today and approaches zero going backward to the beginning of the Universe. The distance between two points in the past would be the comoving distance between them, which is the same as their separation today, multiplied by the scale factor at the relevant time in the past. The scale factor relates to the redshift as,

$$\frac{1}{a} = 1 + z, \tag{1.1}$$

which can be seen easily as $1+z = \lambda_{obs}/\lambda_{em} = a\left(t_{obs}\right)/a\left(t_{em}\right)$. The expansion history of our universe is coded into the scale factor $a(t)$, which results from the solution to a differential equation that involves the time-dependent expansion rate (see §1.3).

The rate of expansion of the Universe is given by the Hubble parameter and is not fixed in time; its value in the past is different from what it is today. This is easily understood by considering the inverse of the Hubble parameter, which gives the light crossing time. Distances in the past were smaller than they are today, and so the light crossing time, and thus the Hubble parameter, must also have been different then. The value of the Hubble parameter today is referenced with a subscript naught, as

H_0, and is otherwise more generally written as H for its other time dependent values in the past. The naught subscript is used throughout this document, as it is generally in cosmology, to distinguish parameter values today from their values in the past. Its explicit formulation as a rate, given in terms of the scale factor, is $H = \frac{1}{a}\frac{da}{dt}$, in which case it is also called the Hubble rate. This formulation follows directly from Hubble's law, $H = v/d$, if we say that $d(t) = d_0 a(t)$, with d_0 being the distance today. This formulation appears in the differential equation that is solved to find the expansion history.

1.3 Framework for Cosmological Models

Cosmological models describe the contents, geometry, and dynamics of the Universe. These are well described by Friedmann's equation (given below, Eq. 1.2),

$$H^2(t) = \frac{8\pi G}{3}\left[\rho(t) + \frac{\rho_{cr} - \rho_0}{a^2(t)}\right]; H_0^2 \equiv \frac{8\pi G \rho_{cr}}{3} \tag{1.2}$$

which is derived by writing down the expansion rate (given by $H = \frac{1}{a}\frac{da}{dt}$) of a simple sphere of matter undergoing isotropic and uniform expansion. The assumptions of uniformity and isotropy are appropriate for the Universe on large enough scales. Making explicit the various forces on the sphere in terms of dimensionless energy densities that are time dependent gives rise to Eq. 1.3,

$$H^2(t) = H_0^2\Big[\Omega_m(t) + \Omega_r(t) + \Omega_k(t) + \Omega_\Lambda(t)\Big]; \Omega_x = \frac{\rho_x}{\rho_{cr}} \tag{1.3}$$

where, Ω_m represents the total matter density, Ω_r is for radiation, Ω_k is for the curvature (geometry) of the Universe, and Ω_Λ represents dark energy. Taking into account how each of these energy densities evolves in time, gives Eq. 1.4,

$$H^2 = H_0^2 \left[\frac{\Omega_{m,0}}{a^3} + \frac{\Omega_{r,0}}{a^4} + \frac{\Omega_{k,0}}{a^2} + \Omega_\Lambda \right], \tag{1.4}$$

or in terms of redshift instead of the scale factor with the relation $a = \frac{1}{1+z}$, we have

$$H^2 = H_0^2 \left[\Omega_{m,0}(1+z)^3 + \Omega_{r,0}(1+z)^4 + \Omega_{k,0}(1+z)^2 + \Omega_\Lambda \right]. \tag{1.5}$$

Dark energy (Ω_Λ) is also parameterized by its equation of state, $w = \frac{P}{\rho}$, which is the ratio of pressure to matter energy density. Although, generally, Ω_Λ can vary with time, in equations Eq. 1.4 and Eq. 1.5 I leave out this dependence which is consistent with the popular choice of dark energy being the cosmological constant. A common parameterization used to assess the time dependence of Ω_Λ, is given by $w(a) = w_0 + (1-a)w_a$ where in w_0 and w_a are constants to be fitted. This formulation checks for first order, or linear, dependence on time.

Equations 1.4 and 1.5 contain six independent parameters that must be specified to describe a complete cosmological model. These include Ω_Λ and four parameters labeled with naughts. The sixth parameter, Ω_b for the baryonic matter, is hidden in the total matter density Ω_m, which includes both dark and baryonic matter. Typically, cosmological measurement techniques are sensitive to a combination of one of these six parameters with an outside parameter construct. For example, a separate parameter that naturally arises in dealing with cluster counts is σ_8, which is the root-mean-square mass fluctuation on scales of eight comoving megaparsecs; this is constrained in combination with the total matter density. The current favored paradigm of ΛCDM cosmology is for a flat universe geometry ($\Omega_{k,0}$=0) with a cosmological constant ($\Omega_\Lambda \neq 0$) and dark matter.

1.4 Distance Measures

We need to know distances to objects, and there are a few different definitions depending on our needs. The comoving distance and the scale factor have already been mentioned above (§1.2). The comoving distance from us to a point in the past, $\chi(a)$, takes into account the expansion of the Universe and is given by the integral, $\chi(a) = \int_{t(a)}^{t_0} \frac{dt'}{a(t')} = \int_a^1 \frac{da'}{a'^2 H(a')}$. The scale factor, $a(t)$, can be assessed observationally by measuring accurate distances to the past, and theoretically, by solving Eq. 1.4.

An observationally motivated distance measure is the angular diameter distance, d_A. This is the distance that relates the known physical size l of an object to the angle θ that it subtends; i.e., $d_A = l/\theta$. Additionally, relating the physical size and angle to the comoving distance, χ, yields the relationship,

$$d_A = a\chi = \frac{\chi}{1+z} \tag{1.6}$$

for a flat universe.

Another observationally useful definition is the luminosity distance, d_L, which is defined to be

$$d_L = \frac{\chi}{a} = \chi(1+z). \tag{1.7}$$

This comes about from considering the observed flux F of an emitter with luminosity L at a sphere of physical radius d, and then considering what happens to this emission in a comoving volume. For a flat universe, these two distances relate to each other as $d_L = d_A/a^2 = d_A(1+z)^2$.

1.5 Hierarchical Structure Formation

The theory of hierarchical structure formation describes the growth of structure in the Universe. It is the idea that matter on smaller physical scales collapses first, under the influence of gravity, followed by matter on larger scales. Small, positive perturbations to a smooth density field in the Universe grow more dense in time. This process results today in an inhomogeneous universe filled with clumps of dark matter, or dark matter halos, with the largest size halos corresponding to clusters of galaxies (and smaller halos to galaxies). Hierarchical structure formation in a ΛCDM cosmology is a fairly successful theory. From this paradigm we have successful predictions of the number distributions of massive halos.

Galaxy clusters, or gravitationally bound units of dark matter, gas and galaxies, occupy the most massive collapsed halos. So, clusters trace the halo distribution in number, mass, and redshift. Cosmological cluster studies today are thus involved in the task of mapping the sky from massive clusters down to low masses, and out to high redshifts. A large and complete sample-volume of clusters contains several cosmological tracers. One of the parameters measured from such data is σ_8, the root-mean-square fluctuation of the matter distribution on the scale of 8 comoving megaparsecs (Mpc). Another parameter is $dN/dM/dz$, the number distribution of clusters in mass and in redshift; this depends on the value of the local Hubble parameter, H_0 (the local rate of expansion), the local relative matter density, $\Omega_{m,0}$, and the geometry of the Universe (e.g., closed, open, or flat). Constraining these parameters from observations requires knowing the cluster masses, numbers, and redshifts. So, next is a discussion of what clusters are made of and how we find them, and also how we measure their masses.

1.6 Clusters

Clusters consist of gravitationally bound galaxies, gas, and dark matter. These components are listed in order of increasing fraction of the total cluster mass. In the hierarchical picture of structure formation, as the dark matter perturbations grew, they attracted and trapped inside them primordial gas. These collapsing structures evolved, forming stars and eventually galaxies. Although some remained isolated, others grew further and attracted and trapped galaxies near their edges. In-falling galaxies and galaxies within the clusters are subject to a harsh environment of gas (Abadi et al. 1999) with which they must interact, and they evolve further. These galaxies lose their gas and new stars quickly through ram pressure stripping (pressure of gas in the surrounding cluster) and through tidal dynamical interactions with other galaxies. This growth process has been modeled and is still an open question in astronomy, along with the formation of galaxies, stars, and the nature (constitution) of dark matter.

1.6.1 Cluster galaxies

The various cluster components and their properties are well known. The historically first observed component is a baryonic one, the galaxies. Clusters with hundreds or more galaxies are considered "rich," while clusters with a few tens are considered "poor" and often called groups. Galaxies are detected in optical or infrared (IR) wave-bands or in spectra, and they are known to be spatially associated through accurate determination of redshift, and thus, three dimensional (3D) distances. Precise redshifts also give the galaxy velocities around a common center, which prove their dynamical association. Clusters typically have a brightest cluster galaxy (BCG) that is coincident with the vicinity of the gravitational center (see review in, Dressler 1984). A large number (though not all) of the galaxies associated with a cluster can also be selected by their color, which is consistent throughout many of the member galaxies. Typical, evolved clusters have most of their galaxies as elliptical galaxies full of old red stars and little to no gas. This evolution is expected to occur on two fronts: through usual aging and interaction with the cluster components. Galaxy members that have evolved thusly are referred to as red sequence galaxies and have been used successfully to find clusters (Gladders & Yee 2001; Koester et al. 2007). Finally, although they were the first component observed, galaxies make up only of order 1% of the total cluster mass, and the remaining percentage consists of the dark matter and the gas.

1.6.2 Cluster gas (the Intra-Cluster Medium)

The second most massive cluster component, composed of baryonic matter, is the intra-cluster medium (ICM), which is gas that permeates the space between galaxies and is bound by the cluster potential. The ICM consists of primordial gas as well as gas stripped or expelled from galaxies that contain heavy metals (e.g., by tidal galaxy-galaxy interactions or supernovae; the term metals here is astronomical terminology that refers to any elements heavier than hydrogen and helium). This gas is tenuous and very hot, with temperatures on the order of $10^7 - 10^8$ Kelvin (from observations and assumption of thermal emission by e.g., Mushotzky et al. 1978). The gas emits in the X-ray due to bremsstrahlung emission and is hot enough to have line emission from ionized species (including iron, see the multiple observational study references in Sarazin 1988).

These hot electrons also interact with the primordial radiation, the CMB, to produce a different kind of observational signature. Photons from the CMB are scattered into higher energies, in an effect known as the Sunyaev-Zel'dovich (SZ) Effect (SZE, Sunyaev & Zeldovich 1970, 1972). The resulting imprint on the CMB is a shift in the temperature of its blackbody spectrum on the order of a few $\sim$mK. In this way, the ICM has two radiation signatures which can be used to detect it and the cluster within which it resides: X-ray emission and the SZE signal on the CMB. Additional known properties of this gas include an increasing temperature profile with radius and a decreasing gas density profile with radius (although there are many observations of this, for one example, Vikhlinin et al. 2009). These two combine with the assumption of hydrostatic equilibrium and virialization to allow modeling of a mass profile. The ICM contributes $\sim 15\%$ to the total cluster mass and so is significantly heavier than the galaxies' contribution.

1.6.3 Cluster dark matter

The dominant cluster component by mass is the non-baryonic (or non-electromagetically interacting) dark matter, which was initially invoked to explain the fact that adding up the masses of the galaxies of a cluster (estimated from their light) does not match the mass estimated from the galaxy velocities (assuming virial equilibrium, see below; Zwicky 1937, 1933). The virial theorem which relates the average kinetic energy of particles to their gravitational potential inside radius R, is given below up to multiplicative constants for reference.

$$KE_{av} \sim PE_{grav} \Rightarrow \frac{1}{2}v^2 \sim \frac{GM\left(< R\right)}{R} \tag{1.8}$$

Cold (or non-relativistic) dark matter (CDM) has since been quite successful in cosmological simulations in predicting structure formation (e.g., Press & Schechter 1974).

Theoretical density profile

The purely gravitational interaction of dark matter particles (in the absence of baryons) has been modeled, resulting in an equilibrium and ubiquitous density profile for describing dark matter halos (e.g., Navarro et al. 1997). A nice result from these studies that supports measured rotation curves and is widely used comes from Navarro et al. (1997); the Navarro-Frenk-White (NFW) profile fits halos well across a large range of masses. Its generalized form is given in Eq. 1.9 below, and it has the same large radius behavior as the 1997 result (r^{-3}).

$$\rho\left(r\right) = \frac{\rho_0}{\left(\frac{r}{r_s}\right)^{-\alpha}\left(1 + \frac{r}{r_s}\right)^{3-\alpha}}. \tag{1.9}$$

The parameter α probes the small-radius behavior of the halo density and, for a value of $\alpha = 1$, matches the 1997 result. The other parameters, ρ_0 (the central density) and r_s (the scale radius), must be fit to individual halos. Variants of the density profile exist, and another commonly used mathematical form includes a central core rather than a cusp, which has a finite density at the origin, for example.

Observing dark matter

Observable signatures of dark matter are those which are sensitive to the total mass (including the baryonic matter). The fraction of dark matter must be determined by accounting carefully for all of the baryonic content. Measures typically used to observe total mass include the velocity dispersion of cluster galaxies, the weak lensing signal, or the cluster temperature under certain assumptions, which are all discussed further below. Weak lensing refers to the phenomenon in which light from background galaxies in the radial vicinity of a cluster is diverted by the large mass or gravity of the cluster, resulting in slight distortions in the shapes of the background galaxies. This effect can be averaged over all background galaxies around a cluster and is proportional to the mass of the cluster, or more accurately, all mass along the line of sight.

1.7 Cluster Detection

Clusters are found through the optical, X-ray, weak gravitational lensing, or SZE signatures of their components discussed above. I discuss below the issues involved with finding clusters through these signatures.

1.7.1 Optical

One way of finding clusters optically is by identifying the member galaxies. Historically, clusters were selected as relative overdensities in the surface number density of galaxies in a region, given a spatial scale and range of magnitudes. Efforts to obtain complete or representative samples of cluster galaxies have resulted in a number of facts being established. The very center of a cluster, for example, typically contains the brightest cluster galaxy (BCG). The surface number density of galaxies is empirically determined to be a decreasing quantity as a function of distance from the cluster center. Additionally, the luminosity function of cluster galaxies, or the number of galaxies between a luminosity of L and $L + dL$, is a decreasing function of the galaxy luminosity (see the many observational study references in Sarazin 1988).

Selection of clusters through member galaxy identification is subject to contamination by background and foreground galaxies, resulting in inaccurate determination of membership and of the number of cluster members. However, understanding how galaxies evolve in the cluster environment has shed light light on better ways of selecting cluster members (Butcher & Oemler 1984). Resulting more improved methods of finding cluster galaxies are discussed next.

Photometric color selection, & redshifts via SED fitting

Multi-band optical imaging (photometry) provides the colors (differences in band fluxes) necessary for identifying a BCG and its corresponding color-associated galaxies, the red sequence. The BCG and its red sequence are more tightly correlated with each other than the surrounding background (or foreground) galaxies, and so this measurement is less plagued by the projection effects mentioned above. This tight relationship, in addition to the member galaxy properties mentioned above, results in a less contaminated set of members and thus provides more accurate cluster properties.

Photometric surveys have also become useful in providing estimates of galaxy redshifts (called photo-z, or z_{ph}) for member identification through spectral energy distribution (SED) fitting (e.g., Budavári et al. 2000). The SED of a galaxy is the optical emission spectrum, and it is fit by averaging it in frequency over typically $3-5$ photometric bands for low or high accuracy. This averaging is done over the full frequency range of the spectrum. As a galaxy spectrum gets redshifted, its overall shape shifts, in addition to shifts in the frequencies of any lines. The changing shape of a redshifted galaxy creates a distribution of fluxes in the observed sub-bands that is different from what would be observed if the galaxy were not redshifted. In this way, the shape of the galaxy spectrum becomes useful, beyond the presence of any line emission (which takes longer observations to find), and is of particular importance when lines are absent. For this reason, full-sky, deep photometric surveys are expected to be the future of optical cluster finding. One drawback of this method is due to catastrophic errors, which refers to the case when very different values of redshift are fitted by the same SED. Another drawback that affects both photometric and spectroscopic (see below) observations is line of sight dust absorption. Dust absorbs light from galaxies differently for the different optical bands and so alters the relative observed flux ratios (or spectral shape) irrespectively of the redshift. In general, photometric surveys are best at finding lower mass systems (where chances of contamination are low) out to high redshift.

Spectroscopy

A highly accurate method of identifying cluster members is through spectroscopy. Redshifts obtained from optical galaxy spectra are typically more accurate than the requirement to be able to definitively associate galaxies physically and to weed out non-members. Although spectroscopy is typically used to follow-up and confirm clusters (perhaps selected through the BCG and companion galaxies associated by color), it has been used to survey the sky in landmark efforts with an offshoot of the Sloan Digital Sky (SDSS), the Baryon Oscillation Spectroscopic survey (BOSS: Dawson et al. 2013).

Obtaining spectra requires longer exposures per galaxy; both of these are reasons why spectroscopy is typically used less frequently to find clusters. Slit masks, however, have relaxed the need to dedicate an entire exposure to a single galaxy. Photometry generally requires shorter exposure times and can be obtained for multiple galaxies in the telescope field of view at once. For large scale studies, photometry thus offers the most amount of usable information.

1.7.2 X-ray

Clusters emit in the X-ray via thermal brehmsstrahlung emission, so their X-ray luminosity scales with the square of their gas density. Due to the relatively large physical sizes of clusters compared to other extragalactic X-ray sources (active galactic nuclei, AGNs), clusters appear in broad (0.2-12 keV) or soft (e.g., 0.5-2.0 keV) band X-ray images as diffuse blobs that are more extended than the point spread function of the telescope. Diffuse X-ray emission is typically unambiguously associated with the emission of a single cluster (no line of sight projection effects). In rare instances, distant (or small) clusters with bright centers can appear to be at the same angular scales as the PSF, causing confusion. A more common occurrence (though it is still rare compared to photometric member galaxy projection contamination) is that of multiple projected AGNs appearing like an extended, diffuse source. At high redshift ($z > 1$) this is a significant problem. These cases require visual and spectral confirmation.

Differentiating clusters from other X-ray sources

As previously mentioned, extra-galactic X-ray sources can be subdivided into two main categories: AGN and galaxy clusters. AGN emit X-rays from the inner regions of their accretion disks or where jets interact with the surrounding material, and their spectra are described by power laws, unlike the cluster gas spectra. Cluster gas emits a thermal bremsstrahlung spectrum, with additional lines from ionized species, depending on the gas temperature. This is the reason why AGN emission is much more compact, especially when compared to cluster scales and why cluster emission is more extended. The extended emission can appear smooth or disturbed depending on the dynamical activity experienced by the cluster. A major advantage of using X-rays to find clusters is largely unambiguous detection. With deep enough observations, temperature profiles or surface distributions can map out dynamical information (e.g., interactions) to which the cluster gas necessarily responds. In this way X-ray observations offer a wealth of information and are crucial to studies of galaxy clusters.

X-rays, and all electromagnetic radiation for that matter, suffer from dimming with distance; this is a consequence of the inverse square law of radiation that arises from redshifting due to the expansion of our Universe. A more distant source will appear fainter at the detector, which means there will be fewer photons above the background available for identification. Another limitation is that there is a lower bound to the mass (which is small) of the cluster (or group of galaxies) that will emit in X-rays; in fact, simulations have indicated that a significant fraction of halos are X-ray dark (Weinberg & Kamionkowski 2003). Thus even an extremely deep observation of the sky will not reveal all clusters present in the region. An additional limitation is the long exposure time, typically on the order of 10s of kilo-seconds. Optical observations required to identify clusters are much shorter by comparison. Due to the low X-ray event rate and small effective area of current X-ray telescopes, clusters must be observed on the order of hours to obtain reliable information from their X-ray data. Considering together the strengths and limitations, it can be said that X-rays most effectively find relatively compact clusters at lower redshifts which are generally also massive.

1.7.3 Weak Lensing

The minor distortions to the shapes of background galaxies (the shear) as seen in optical images produced by small deflections of the background light relatively far away from a massive object along the line of sight is the effect known as weak lensing. The amount of shear produced is proportional to the projected mass along the line of sight and diminishes farther away from the lensing mass. Figure 1.1 shows a schematic of this distortion, focusing in particular on how a circular galaxy's shape changes closer to the cluster center. For comparison, the cluster in the figure is one which has a nearly complete Einstein ring from strong gravitational lensing.

The fundamental principle behind detecting a weak lensing signal is the assumption that on large enough spatial scales, or rather across the whole sky, there is no preferred galaxy orientation. So in contrast, galaxy shapes averaged near massive clusters would be non-circular and oriented in a preferential direction due to their weak lensing magnification (see Mellier 1999, for a review). Key requirements for

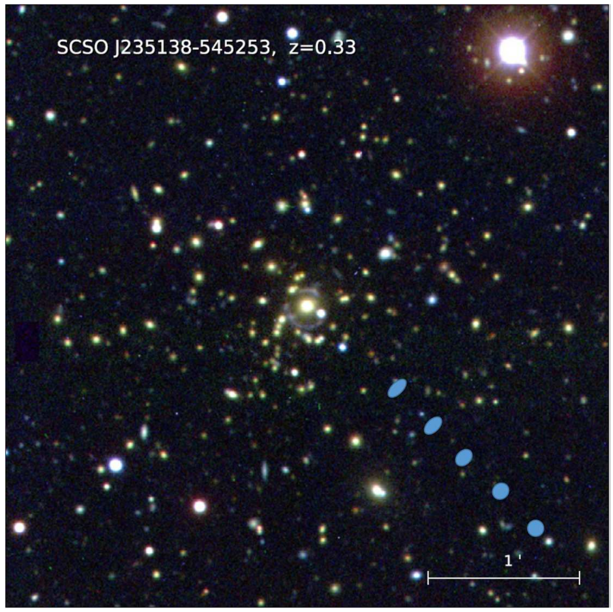

Figure 1.1 Weak lensing effect schematic. The background is the named cluster discovered in the Southern Cosmology Survey (Menanteau et al. 2010a) at Rutgers; it has a strong lensing arc around its central BCG. Far away from where the arc occurs, or the strong lensing regime, background circular galaxies are weakly lensed and are less sheared and so appear to have lower ellipticities. This effect is illustrated by the blue ellipses which show the increased shear on a circular background galaxy with decreasing distance from the cluster center (which would eventually approach the strong lensing limit)

high resolution measurements of the shear and its spatial variation are a large background galaxy number density and accurate shape measurements. Peaks of the shear profiles indicate locations of large projected mass. The treatment of redshifts is also important, as the shear is maximum for ratio of observer-to-lens and lens-to-source galaxy distances near unity and lower for all other distance ratios. So it is important to have some way to assess this difference in shear due to the source galaxy redshift.

The sensitivity of weak lensing to the cluster mass, which is the fundamental property of interest, is an attractive attribute for doing cluster cosmology. However, the sensitivity being to all mass along the line of sight is a problem for estimating individual cluster masses. If unaccounted for, line of sight structure is a significant source of contamination. Simulations quantify this contamination at the $\sim 20\%$ level (Becker & Kravtsov 2011). A fortuitous result however, is that the estimated masses are expected to be unbiased. On the other hand, there is some evidence for X-ray

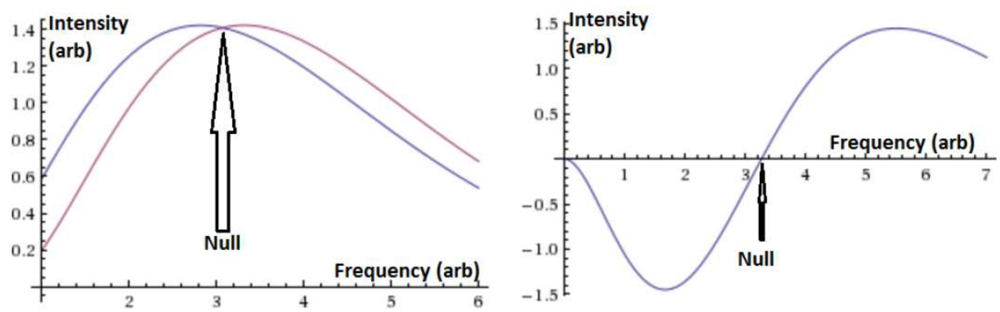

Figure 1.2 Schematic showing the incident and shifted CMB curves (left) in arbitrary units, along with their difference (right).

mass estimates to be biased low (e.g., von der Linden et al. 2014a). Regardless, there is expected to be a large intrinsic scatter. Finally, the redshift dependence of the lensing signal limits its usefulness in finding clusters, since there will be a small number of source galaxies that are roughly twice the distance between us and the lens, and therefore, this lowers number of galaxies available for constraining the weak lensing signal (e.g., Wittman et al. 2014). Weak lensing selection should find intermediate to high mass systems (limited by line of sight structure contamination) over intermediate redshifts (irrespective of the cluster dynamical state). In Chapter 2, I present my efforts in characterizing selection by weak lensing; which is a young field.

1.7.4 Sunyaev-Zel'dovich Effect

The Sunyaev Zel'dovich Effect (SZE: Sunyaev & Zeldovich 1970, 1972) refers to distortions to the CMB temperature produced by inverse Compton scattering by the hot cluster ICM. When CMB photons inverse Compton scatter off of a thermal distribution of electrons (the ICM), their spectrum shifts toward higher frequencies (to the right), providing a unique spectral signature for finding clusters. The scattered CMB spectrum is higher in intensity relative to the incident spectrum to the right of their intersection, called the null frequency (see Figure 1.2 for a schematic). Conversely, to the left of the null, there is an intensity decrement relative to the background spectrum (see Carlstrom et al. 2002, figure 2). Simply imaging the sky at the frequency of the peak decrement, for example, would show holes in the sky map where the clusters are. Further confirmation of the cluster is obtained by imaging additionally at both the null frequency and the peak increment frequency, which would show no difference at the cluster position in the null map but a bright spot in the increment map.

The shifted intensity spectrum can be modeled as a small temperature distortion ($\sim 1mK$) to the incident CMB. The fractional energy gained per photon from collisions along the line of sight is given by the Compton y-parameter below:

$$y = \int \frac{k_B T_e}{m_e c^2} n_e \sigma_T dl. \tag{1.10}$$

This is the integral along the line of sight of the fractional energy ($k_B T_e/m_e c^2$) gained from each scattering electron times the effective number of electrons along the line of sight ($\int n_e \sigma_T dl$); here, n_e is the electron number density, T_e is the electron temperature, and σ_T is the Thompson scattering cross section. The SZE temperature distortion relates to the y parameter as below for non-relativistic electrons (Sunyaev & Zeldovich 1970):

$$\frac{\Delta T_{SZE}}{T_{CMB}} = y \left(x \frac{e^x + 1}{e^x - 1} - 4 \right) \tag{1.11}$$

where $x = h\nu/kT_{CMB}$ is the dimensionless frequency. This effect is thus independent of redshift and particularly useful for probing the high redshift Universe, where other methods (e.g., optical or X-ray) suffer from dimming.

The integrated SZE signal (denoted typically as Y_{SZE}) is the temperature distortion integrated over the solid angle (dA/D_A^2):

$$Y_{SZE} \equiv \int \Delta T_{SZE} \, d\Omega \sim \frac{N_e \langle T_e \rangle}{D_A^2} \sim \frac{M_g \langle T_e \rangle}{D_A^2} \sim \frac{M \langle T_e \rangle}{D_A^2} \tag{1.12}$$

The integrated signal is thus proportional to the total number of electrons in the cluster, or the mass, but weighted by the average temperature. This presents a few observational consequences. For one, because of the dependence on angular diameter distance, the integrated signal now depends on redshift ($D_A = \chi/(1+z)$), at least until at high redshift ($1 \lesssim z \lesssim 2$) when this distance becomes approximately flat (Wright 2006). A second consequence is that if a cluster of a certain mass can be seen through its SZE signal at high redshift (where D_A is approximately flat), then a cluster of the same mass at higher redshifts is a also visible through the SZE. This is because at higher redshifts the Universe is relatively more dense, and the greater density results in a larger compton y parameter value (Eq. 1.10) and a consequently greater SZE signal (Eq. 1.12) for the cluster of the same mass. In this way, the ability to provide a mass limited sample independent of redshift is one of the biggest strengths of SZE cluster selection (for virial equilibrium, mass scales with temperature as $M \sim T^{3/2}$).

New large area millimeter wave telescopes have come online to find clusters and more information about the CMB on smaller angular scales. Two ground based telescopes that are optimized to find clusters are the Atacama Cosmology Telescope (ACT Fowler et al. 2010) and the South Pole Telescope (SPT: Ruhl et al. 2004). The Planck satellite (Planck Collaboration et al. 2015) completed its full sky survey in the SZE with a top tier goal of finding clusters. The biggest challenge for the ground based telescopes is to model the atmosphere, which is an unpredictable time-varying component. The data analysis is still changing, and improving, but nonetheless, ACT, SPT and *Planck* have all successfully identified and confirmed new massive clusters for cosmology. Clusters found through the SZE tend to be massive and are found out to large redshifts. I derived X-ray properties from a sample discovered by ACT (chapter 3).

1.8 Cluster Mass Determination

As previously stated, the various observational signatures of the cluster components relate to the total cluster mass. I discuss below the fundamental and extrapolated ways from which we typically determine mass today from the cluster observables. Note that although weak lensing is done with optical data, I list it as a separate method and subsection below.

1.8.1 Optical

The most direct way to determine mass optically is by measuring the galaxy velocities in three dimensions and to assess them as tracers of the gravitational potential and thus the total cluster mass. The most common usage of galaxy velocities is in determining the root-mean-square (rms) velocity dispersion, σ.

Dispersion

The galaxy velocity dispersion relates to the total cluster mass through the virial theorem, resulting in the relationship below:

$$M \sim \frac{R\left\langle v^2\right\rangle}{G} = \frac{R3\sigma_r^2}{G} \tag{1.13}$$

for an isotropic system, where G is the gravitational constant, $\sqrt{\langle v^2\rangle}$ is the average three dimensional velocity dispersion, and σ_r is the radial velocity dispersion, which is what we observe. The isotropic assumption is a fundamental limitation of this method because velocities in the plane of the sky cannot be measured for cluster scale systems.

Richness

A naive or informed (by dark matter simulation) expectation would suggest that the more massive a cluster is, the more galaxies may be trapped in it. Power law scaling relations between total cluster mass and richness have been empirically fit (with an additional optional dependence on the BCG luminosity, see, e.g., Reyes et al. 2008, who used stacked weak lensing masses). Dynamical mass estimates are also commonly used to calibrate optical relations to cluster mass. The Sloan Digital Sky Survey (SDSS), which made it possible to obtain multiple optical spectra quickly from a single observation, has been an ideal tool for such investigations and has been used to publish empirical scaling relations between richness and mass. An inherent limitation of richness-based mass estimation would be due to the statistics of structure formation (that is, not every cluster sized halo of mass M_{cl} would trap within it an identical number of galaxy sized halos N_{gal}). Practically however, galaxy member contamination by foreground or background galaxies is still an issue.

Optical luminosity

Similar to the richness, a power law scaling relation was defined by Reyes et al. (2008), between total cluster mass and the optical luminosity (again with an optional additional dependence on the BCG luminosity). Optical luminosity is defined as the total band-limited luminosity of all galaxies within a specified radius (e.g., R_{200}, or the radius within which the mean mass density of the cluster is 200 times the critical density of the universe). A relationship with optical luminosity probes how well the star formation in the cluster galaxies traces the total cluster mass.

1.8.2 X-ray

The fundamental sensitivity of X-rays to cluster mass comes from the virial theorem, relating the cluster temperature (estimated with X-rays), as a measure of the average kinetic energy, to the total cluster mass, which relates to the potential (see subsection below on scaling laws). Additional relations between total mass and other cluster observables are derived under certain assumptions as well.

Scaling Laws: M_g, T_X, Y_X

Assuming self-similar and scale-free growth of clusters, a number of relationships can be inferred between cluster properties at any redshift. The total cluster mass M, for example, is defined to be inside the virial radius R, which is determined as the radius of a fixed overdensity with respect to the critical density of the universe (e.g., $M/\frac{4}{3}\pi R_{200}^3 = 200\rho_{crit}$, see Press & Schechter 1974). And so, we have for any cluster or virialized halo that $R \sim M^{1/3}$. Furthermore, expressing the average kinetic energy in the virial theorem as temperature, T, we have that $T \sim M/R$. Combining this with the relation between M and R above, we get that

$$M \sim T^{3/2}. \tag{1.14}$$

In general, we additionally expect the gas mass to be a fixed fraction f_g ($f_g \propto \Omega_b/\Omega_m$) of the total mass:

$$M_{tot} = f_g^{-1} M_g \tag{1.15}$$

The SZE signal, which is related to mass, is a measure of the total thermal energy, obtained by integrating the gas density and temperature, as seen above (§1.7.4). So, $Y_{SZE} \sim M_g T_g \sim M M^{2/3} = M^{5/3}$. Since the gas density and temperature can also be determined with X-rays, a purely X-ray measure of the total thermal energy, Y_X, is defined by multiplying the gas mass by the average temperature ($Y_X \equiv M_{g,X}T_X$, Kravtsov et al. 2006). This scales with total mass in the same way as the SZE signal:

$$M_{tot} = Y_X^{3/5} \tag{1.16}$$

This is, in principle, a more robust mass estimator (than for example the gas mass fraction) because its components, M_g and T_g, have opposite systematics.

Hydrostatic Modeling

Assuming hydrostatic equilibrium for the cluster gas, which is reasonable if the cluster is isolated, it is possible to relate the gas temperature profile $T_g\,(r)$ and gas density profile $n_e\,(r)$ to the radial total mass profile as below:

$$M\,(r) = -\frac{kT_g\,(r)\,r}{\mu m_p G}\left(\frac{d\ \ln\ n_e}{d\ \ln\ r} + \frac{d\ \ln\ T_g}{d\ \ln\ r}\right) \tag{1.17}$$

Both the gas density and temperature profiles can be constrained by the cluster observations with sufficient data.

1.8.3 Weak Lensing

The observed shear profile is fitted to a model that predicts shear based on an underlying mass (density) profile. Masses within desired radii are subsequently determined from the model mass profile. An important source of uncertainty for such estimates is additional line of sight structure, as the measured galaxy shapes respond to all structure between us and the source galaxy. This is an inherent limitation of weak lensing, which can be improved, but not necessarily eliminated, by considering source galaxy redshifts. Although masses from weak lensing are expected to be unbiased (see von der Linden et al. (2014b) for a recent discussion, or Becker & Kravtsov (2011) for simulations), there is some evidence for X-ray masses to be biased low (e.g., von der Linden et al. 2014a).

1.9 Cosmology from clusters

Clusters offer a number of ways to determine cosmological parameters. The most common and directly related to cosmology is cluster counts. A review of the cosmological parameter constraints that clusters can achieve is given by Allen et al. (2001).

1.9.1 Cluster counts: $dN/dM/dz$.

The mass function, or the number of clusters between mass M and $M + dM$ at any given epoch, has been theorized and shown via simulations to depend on the matter density Ω_m and the root-mean-square mass fluctuation σ_8 (e.g., Press & Schechter 1974; Bahcall & Fan 1998). Furthermore, the evolution of this mean mass fluctuation is sensitive to the growth function (which depends, e.g., on dark energy). As an example of this, Dodelson (2003) shows that a no dark energy and flat geometry model (CDM) predicts hundreds fewer clusters in the past relative to today than does a ΛCDM model. That means that the number of clusters grows more slowly (from intermediate redshift to today) in the presence of dark energy.

The high mass end of the mass function provides strong constraints on cosmology, as very few clusters are expected to have high mass, particularly at high redshift. SZE surveys are ideal to identify such systems due to the lack of redshift dependence of the integrated SZE signal, particularly at high redshift. ACT and SPT have identified a few such high-redshift high-mass clusters (e.g., Menanteau et al. 2013; Vanderlinde et al. 2010). I contribute X-ray follow-up to Menanteau et al. (2010b, described in chapter 3), to determine properties of clusters with available X-ray data.

1.9.2 Cluster gas mass fraction: f_{gas}

The baryon fraction of the Universe can be estimated from the cluster gas mass fraction. The basic idea is that a collapsed halo traps within it primordial gas, some of which gets funneled to the center, and the rest of which participates in star formation within galaxies. For massive clusters, less than $\sim 10\%$ of the mass is foundd to be in the cluster gas. These methods have been incorporated by, for example, Allen et al. (2008).

1.10 X-ray Analysis

Here, I describe some of the basics of X-ray analysis with *XMM Newton* (and *Chandra*) for reference in the later chapters. As previously mentioned, the current generation of X-ray telescopes focuses X-rays onto the detectors using cylindrical grazing incidence mirrors. Generally, the X-ray event (or photon incidence) rate is low enough (typical of galaxy clusters) that each incoming photon gets read out from the CCD's before another strikes. Each photon can thus be associated with not only its two dimensional position and time of incidence, but also its energy. For very bright sources, this condition fails and multiple photon strikes within a single read-out, called detector pile-up, must be dealt with during analysis. The X-ray data are available as a data meta-cube, which is a data structure with four "dimensions"; one "dimension" records the X position of the photon, one dimension records the Y position, one records the time of incidence, and the final records the photon energy. Integrating the meta-cube along the various, individual or multiple, dimensions allows for calculations of fluxes, light-curves, exposures, images, and spectra.

1.10.1 *XMM Newton*

The *XMM Newton* telescope has two types of detectors (cameras) at the foci of three co-aligned telescopes. The `MOS` (metal oxide semi-conductor) and `pn` (named for its use of p- and n- type semi-conductors) cameras have relatively different energy responses, sensitivities, chip geometries and read out times. Each `MOS` camera has six chips, (two of which for `MOS1` are dead since 2005 and 2012), and the `pn` camera has 12 chips. Their energy calibrations require continual monitoring and updating in the calibration files (e.g. due to degradation from environmental impacts, or temperature sensitivity of the electrons). For this reason, it is important to re-apply the calibration with the newest files to any processing of new or old data.

In general, energy calibration is assessed for each analyzed source by generating two files, the effective area, and the energy redistribution matrix. The effective area is the detector area folded with the energy dependent response of the detector and is called the *ancillary response function*, or `arf`. The energy redistribution matrix, or `rmf`, accounts for the spread of energy of incoming monochromatic light, which arises from effects such as the quantum nature of the read-out (or the energy resolution) and charge losses. These two functions are essential to ensure good energy calibration and accurate determination of uncertainties.

Additional analysis considerations include effects such as vignetting. Vignetting is the reduction in the effective area with radial distance from the telescope axis due to reduced illumination near the edges (collimated incident light does not illuminate the detector evenly due to blockage from the nested mirrors). This is folded into the `arf`, but can be assessed by making a map of the total exposure of each detector pixel.

1.10.2 X-ray backgrounds

Internal telescope background arises from cosmic-rays. Cosmic-rays ionize material around the detectors which fluoresces or produces radiation that then lands on the detector. This can be carefully determined with blank sky observations in which the camera is covered. The typical spectral dependence of such background is determined from “canned” (already observed, or determined) observations. It can also be estimate like the unresolved astrophysical background discussed below.

Astrophysical background consists of distant unresolved sources whose spectra and fluxes are estimated for each observation by analyzing source-free regions. Another astrophysical source of the X-ray background is soft proton flares (with energies less than 100 keV). Soft protons trapped in some regions of the earth’s magneto-sphere are funneled into the telescope with high event rates and varying spectral distributions. Data during periods of soft proton flare activity cannot be modeled and must be discarded. These periods can be identified from the high energy count rates where no significant source emission is expected.

Chapter 2

A Weak lensing Selected Cluster Sample[1]

2.1 Introduction

The power of finding clusters directly through the fundamental cosmological quantity, the cluster mass, was recognized by early weak lensing studies (Tyson et al. 1990; Kaiser 1992). Weak lensing selects solely on the mass along a line of sight and is independent of physical processes that can affect our observations of the baryonic components (e.g., mergers). A large number of individual clusters have been studied in shear, but there have been fewer studies of shear-*selected* clusters (Wittman et al. 2006; Miyazaki et al. 2007; Gavazzi & Soucail 2007; Schirmer et al. 2007; Miyazaki et al. 2015). The first set of clusters selected in shear was published by Wittman et al. (2006) from the Deep Lens Survey (hereafter DLS; Wittman et al. 2002).

Although there have been numerous weak lensing follow-up studies of X-ray or optically selected samples, follow-up efforts that focus on characterizing the properties of weak lensing selected clusters are few in the literature (e.g., Giles et al. 2015, 10 clusters). Our work with the DLS falls in this latter camp.

We continue the study of the shear-selected clusters discovered in Wittman et al. (2006). These are 7 of the 8 highest ranked shear peaks in the first 8.6 deg^2 of the 20 deg^2 DLS. The top ranked shear peak among them corresponds to the previously

[1]This chapter largely contains work that was submitted to the Astrophysical Journal in August 2016 as the paper titled "X-ray Temperatures, Luminosities, and Masses from XMM-Newton Follow-up of the First Shear-selected Galaxy Cluster Sample" by Deshpande et al. (2016). The most up to date version of this work will appear in the journal.

known complex of clusters associated with Abell 781. This complex has been previously studied in detail, both in X-rays and in weak lensing with emphasis on mass comparison (Sehgal et al. 2008; Wittman et al. 2014). The fifth ranked shear peak was deemed to be a line of sight projection, while the remaining 6 have all been confirmed as clusters. The majority of the shear peaks show multiple X-ray and optical (in the DLS) counterparts (Wittman et al. 2006).

The initial follow-up to confirm the shear peaks as clusters was conducted by Wittman et al. (2006), using low exposure *Chandra* imaging. We have since been awarded *XMM Newton* data, with which we can learn more by examining the sample in some of the best studied (and low scatter) X-ray properties: L_X, the X-ray luminosity, and T_X, the X-ray temperature (e.g., Vikhlinin et al. 2009; Pratt et al. 2009; Mantz et al. 2010). We can examine them as mass proxies (Ettori 2013) and study their behavior along X-ray scaling laws (e.g., Pratt et al. 2009; Maughan et al. 2012; Mahdavi et al. 2013), which are typically low in scatter and drawn from self-generated properties.

In this study we determine X-ray temperatures, luminosities, and masses. Our sample covers the same survey area as Wittman et al. (2006), hereafter `W06`, but goes further into the distribution of shear, adding three more peaks. Some of the DLS fields in our study (in particular F2) have previously been examined, in part or in entirety, by other studies (Kubo et al. 2009; Utsumi et al. 2014; Miyazaki et al. 2015; Geller et al. 2010; Starikova et al. 2014; Ascaso et al. 2014); we discuss them in the context of our own work in section §2.2.2 below. Our study includes DLS fields F2-F5, encompassing a larger survey area than these other studies. We focus on the X-ray properties of the sample, showing the $L_X - T_X$ relation for the first time and comparing it to other X-ray selected cluster samples. We obtain X-ray mass estimates using temperature as a proxy which we compare to weak lensing masses determined by the DLS team (Abate et al. 2009; Wittman et al. 2014).

Table 2.1 *XMM-Newton* observations.

No.	Name	OBS_IDS	Duration (s) PN	Duration (s) ⟨MOS⟩	Exposure (s) PN	Exposure (s) ⟨MOS⟩
1.	DLSCL J0920.1+3029	0150620201$^{(a)}$	13230	16173	11709	14466
		0401170101	68695	78230	52107	67687
2.	DLSCL J0522.2−4820	0303820101	34700	41572	8943	24265
3.	DLSCL J1049.6−0417	$^{(b)}$	...	...	...	...
4.	DLSCL J1054.1−0549	0552860101	51128	53208	29092	36667
5.	DLSCL J1402.2−1028	$^{(b)}$	...	...	...	...
6.	DLSCL J1402.0−1019	$^{(b)}$	...	...	...	...
7.	DLSCL J0916.0+2931	0303820301	39937	41572	16982	23393
8.	DLSCL J1055.2−0503	0303820201	34933	36572	28309	30876
		Averages:-	40437	44544	24254	32892
Beyond the initial Wittman et al. (2006) publication:						
B9.	DLSCL J1048.5−0411	0150620901	12036	13672	10167	12310
B10.	DLSCL J0921.4+3013	0150620101	11268	15781	8936	13000
B11.	DLSCL J0916.3+3025	0152060301	11605	10239	8605	9142
		Averages:-	11636	13231	9236	11484

NOTE:- Column (1) gives the DLS candidate number from `W06`, or designations beginning with the letter B that we assign here to the *beyond* subset. 'Duration' reports the total telescope on-time. 'Exposure' shows the total exposure after background flare filtering. '⟨MOS⟩' gives the average value from the two mos cameras. An (a) indicates the observation is analyzed in Sehgal et al. (2008). A (b) indicates there is no corresponding *XMM Newton* data; initial *Chandra* follow-up (`W06`) found no X-ray counterpart to peak 5, and found very low signal-to-noise X-rays corresponding to peaks 3 and 6.

This chapter is organized as follows. The X-ray data, its analysis and the cluster properties are discussed in section 2.2. The luminosity-temperature relation is presented in §2.2.6. The X-ray mass estimates and comparison to weak lensing are discussed in section 2.3. We conclude with a summary in §2.4. Throughout this chapter we use $H_0 = 70$ km s^{-1}Mpc^{-1}, $\Omega_\Lambda = 0.7$ and $\Omega_m = 0.3$ and report all uncertainties at the 1σ confidence level.

2.2 The Sample, X-ray Data, & Analysis

Our shear-selected sample comes from the *XMM Newton* follow-up of shear peaks discovered in the initial 8.6 deg^2 analysis of the DLS (fields F2-F5, `W06`). We discuss the X-ray observations of eight shear peaks. Five of them are highly ranked in shear and had enough signal-to-noise in early *Chandra* follow-up (`W06`) to be awarded deep *XMM Newton* observations. We add three more DLS shear peaks that go lower into the distribution of shear than went the 2006 publication; these were awarded shallower *XMM Newton* observations to confirm as clusters. The specific observations (PI: J. P. Hughes) are listed in Table 2.1 with their observation identifiers (obsIDs) and exposures. Our follow-up naturally divides here into two subsets, as the five shear peaks from the 2006 paper, hereafter referred to as the original subset, are observed at greater depth ($\langle t_{exp} \rangle$ = 22ks) than the remaining three ($\langle t_{exp} \rangle$ = 10ks), hereafter called the *beyond* subset. For both of these subsets we determine the X-ray properties, and for the *beyond* subset, we additionally report the association of the X-ray clusters to the shear peaks.

Nearly every shear peak has associated with it more than one X-ray cluster, a likely consequence of the high smoothing in the DLS shear maps. Some of the clusters that are farther from the shear peaks are detected at lower significance in the X-ray and so we cannot determine the full set of properties for all of them. For clarity, we include a diagram in Figure 2.1 which shows how the X-ray clusters belonging to the original and *beyond* subsets subdivide according to the properties we are able to determine for them. Also referenced in the diagram, are serendipitous X-ray clusters that we find in the observations; these are clusters that could not be confidently associated to the shear peaks. We describe, next, our identification and detection of the X-ray clusters in the *XMM Newton* data, beginning with the imaging required to do so.

2.2.1 Imaging

We generated images in the soft 0.5-2.0 keV band using *XMM Newton* data products available through the *XMM-Newton Pipeline Processing System* ($XMM{-}PPS$). In particular, we co-added the 0.5-1.0 keV and 1.0-2.0 keV band images, background maps, and exposure maps respectively, and from all three cameras to create a single background-subtracted, exposure-corrected image per observation. When relevant, we co-added our 0.5-2.0 keV images from multiple observations (ObsIDs) resulting in one soft-band X-ray image per DLS shear peak. X-ray counterparts were identified

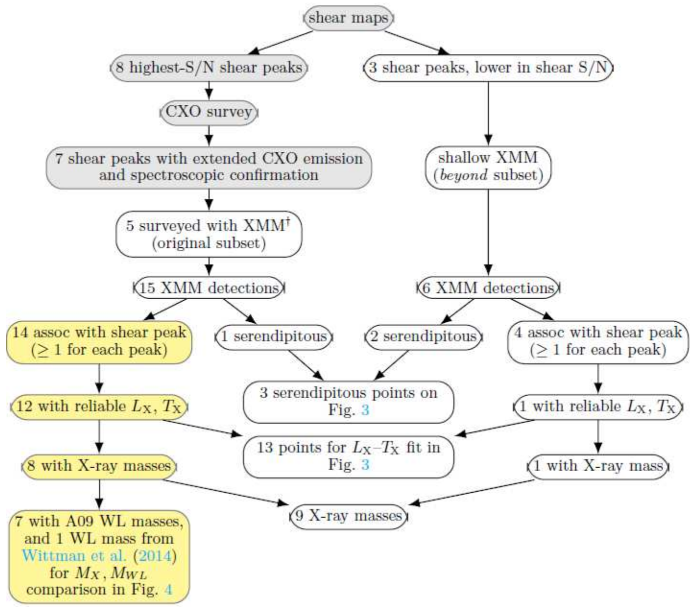

Figure 2.1 Subdivision of our shear-selected clusters by X-ray properties. Grey shaded boxes at the top differentiate the work completed in W06. Yellow shading in the lower left branch highlights the information that results in our mass comparison (§2.3.3, Figure 2.10). The categories for individual clusters are given in Table 2.2.
† See caption in Table 2.1.

on these images, and they were also used to specify regions for spectral extraction. These processing steps are described in the following sections.

2.2.2 Source Detection

We recover *XMM Newton* emission from nearly all of the X-ray clusters that were identified in W06 and were associated to the DLS shear peaks. See Table 2.2 for a list. Two of these could not be included in our analysis due to contamination of their X-ray signal. The central counterpart to DLSCL 0916.3+2931, CXOU J091554+293316, is heavily confused with a known point source (in the wings of the *XMM Newton* point-spread-function, see Figure 2.2). The emission of the subcluster of Abell 781 (CXOU J092011+302954, W06; Sehgal et al. 2008), is confused with the main cluster's emission with which it is likely merging. Excluding these two, the detection properties of the remaining recovered sources are given in Table 2.2, several of which are imaged in Figure 2.2.

Table 2.2 X-ray clusters in the *XMM Newton* observations of DLS shear peaks.

No.	Name	XMM_IDS	Region ′(kpc)	Rate (10^{-3}cts s^{-1})	Significance	Subdivision by properties (7)	(8)	(9)	(10)	(11)
1.	DLSCL J0920.1+3029	CXOU J092026+302938	3.85(1034)	857 ± 4	197	✓	✓	✓	✓	✓
		CXOU J092053+302800	2.57(672)	164 ± 2	74	✓	✓	✓	✓	✓
		CXOU J092110+302751	2.27(761)	53 ± 2	33	✓	✓	✓	✓	✓
		CXOU J092011+302954$^{(a)}$	...	...	...	✓	no	no	no	no
		XMMU J091935+303155	2.17(728)	116 ± 2	62	✓	✓	✓	✓	TBD
2.	DLSCL J0522.2−4820	CXOU J052215−481816	2.19(580)	443 ± 9	47	✓	✓	✓	✓	✓
		CXOU J052159−481606	1.60(424)	87 ± 6	15	✓	✓	✓	no	no
		CXOU J052147−482124	0.67(177)	3.9 ± 1.4	3	✓	✓	✓	no	no
		CXOU J052246−481804	1.17(241)	20 ± 3	7	no	✓	no	no	no
4.	DLSCL J1054.1−0549	CXOU J105414−054849	1.25(238)	32 ± 1	23	✓	✓	✓	✓	✓
7.	DLSCL J0916.0+2931	CXOU J091551+293637	1.30(491)	17 ± 1	12	✓	✓	✓	no	no
		CXOU J091601+292750	1.08(408)	37 ± 2	22	✓	✓	✓	✓	✓
		CXOU J091554+293316$^{(b)}$	...	...	...	✓	no	no	no	no
8.	DLSCL J1055.2−0503	CXOU J105535−045930	1.00(404)	23 ± 1	20	✓	✓	✓	✓	✓
		CXOU J105510−050414	1.26(534)	28 ± 1	22	✓	✓	✓	no	no
Beyond the initial Wittman et al. (2006) publication:										
B9.	DLSCL J1048.5−0411	(B9a) XMMU J104817−041233	2.10(488)	77 ± 3	22	✓	✓	✓	✓	TBD
		(B9b) XMMU J104806−041411	0.83(222)	17 ± 2	11	no	✓	no	no	no
B10.	DLSCL J0921.4+3013	(B10a) XMMU J092124+301324	0.60(n/a)	5.0 ± 1.6	3	✓	no	no	no	no
		(B10b) XMMU J092118+301156	0.66(n/a)	4.4 ± 1.9	2.4	✓	no	no	no	no
		(B10c) XMMU J092102+300530	0.88(332)	15 ± 2	10	no	✓	no	no	
B11.	DLSCL J0916.3+3025	(B11a) XMMU J091607+302724	1.17(486)	21 ± 2	10	✓	✓	no$^{(c)}$	no	no
					Totals:	18	17	13	9	TBD

NOTE:- The *beyond* subset parenthetical labels are referenced in §2.2.2. A (n/a) is placed where no physical radius can be determined due to lack of redshift. Column (7) marks the X-ray clusters that *can* be confidently associated to DLS shear peaks (§2.2.2). Column (8) marks clusters with sufficient statistics to constrain L_X and or T_X (see Table 2.3 and §2.2.4). Column (9) marks the clusters included in the $L_X - T_X$ fit. Column (10) marks the clusters for which an X-ray mass could be determined (§2.3.1). Column (11) marks the clusters with both X-ray and weak lensing masses (§2.3.2).

$^{(a)}$ Subcluster of the main cluster of Abell 781 (Sehgal et al. 2008); emission is confused with the main component.

$^{(b)}$ Central of 3 X-ray counterparts to DLSCL J0916.0+2931; emission is heavily confused with a known point source.

$^{(c)}$ Not included in fit because T_X could not be constrained (see Table 2.3).

For the three *beyond* subset shear peaks, we identify potential X-ray counterparts by using the *XMM−PPS*. On the raw data with updated calibration, we re-run the *XMM Newton* pipeline which performs its own wavelet decomposition based source detection. The resulting source list is a combined list from source detection performed in multiple bands (soft, and hard) from each camera. We verify the extended sources from this list by eye on our soft band images and list them in Table 2.2 as potential counterparts along with their detection properties.

Beyond **subset associations**

In the rest of this section we discuss the association of these potential X-ray counterparts to the *beyond* subset shear peaks, referencing any available optical information (from the DLS, or elsewhere). The shear peaks in this subset were identified in early work with the DLS (around 2002) and we targeted them for *XMM Newton* observation; however, they did not make the cut for inclusion in W06. The most significant X-ray detection in the *beyond* subset is associated with DLSCL J1048.5-0411, which is previously unpublished; we discuss its association in the next paragraph. The remaining two *beyond* subset shear peaks have appeared previously in the literature: they are located in DLS field F2, which has been repeatedly studied with new observations in different wave-bands and new weak lensing analyses. We include these in the context of associating the shear to the X-rays further below.

DLSCL J1048.5-0411, as part of the *beyond* subset, is a lower signal-to-noise detection in shear. There are two extended X-ray sources detected at high significance, located $\sim 3.5'$ (B9a) and $\sim 7'$ (B9b) away toward the southwest of the DLS position. The emission of the former (nearby) X-ray source lies in an extended high shear region which supports their likely association despite the large offset between the peaks. Visual inspection of the DLS data reveals an optical cluster with a brightest cluster galaxy (BCG) that is well centered on the X-ray peak. We obtained redshifts of galaxies near this BCG as part of the campaign described in W06. We observed the cluster with the Low-Resolution Imaging Spectrograph (Oke et al. 1995) on the Keck I telescope in April of 2005 and obtained secure redshifts of sixteen galaxies. We found eleven galaxies to be likely members, with a mean redshift of 0.2463 ± 0.0006. The X-ray emission of this nearby source fits well to a model of thermal cluster emission at this redshift.

For the second X-ray source, $\sim 7'$ from the shear peak, the optical association in

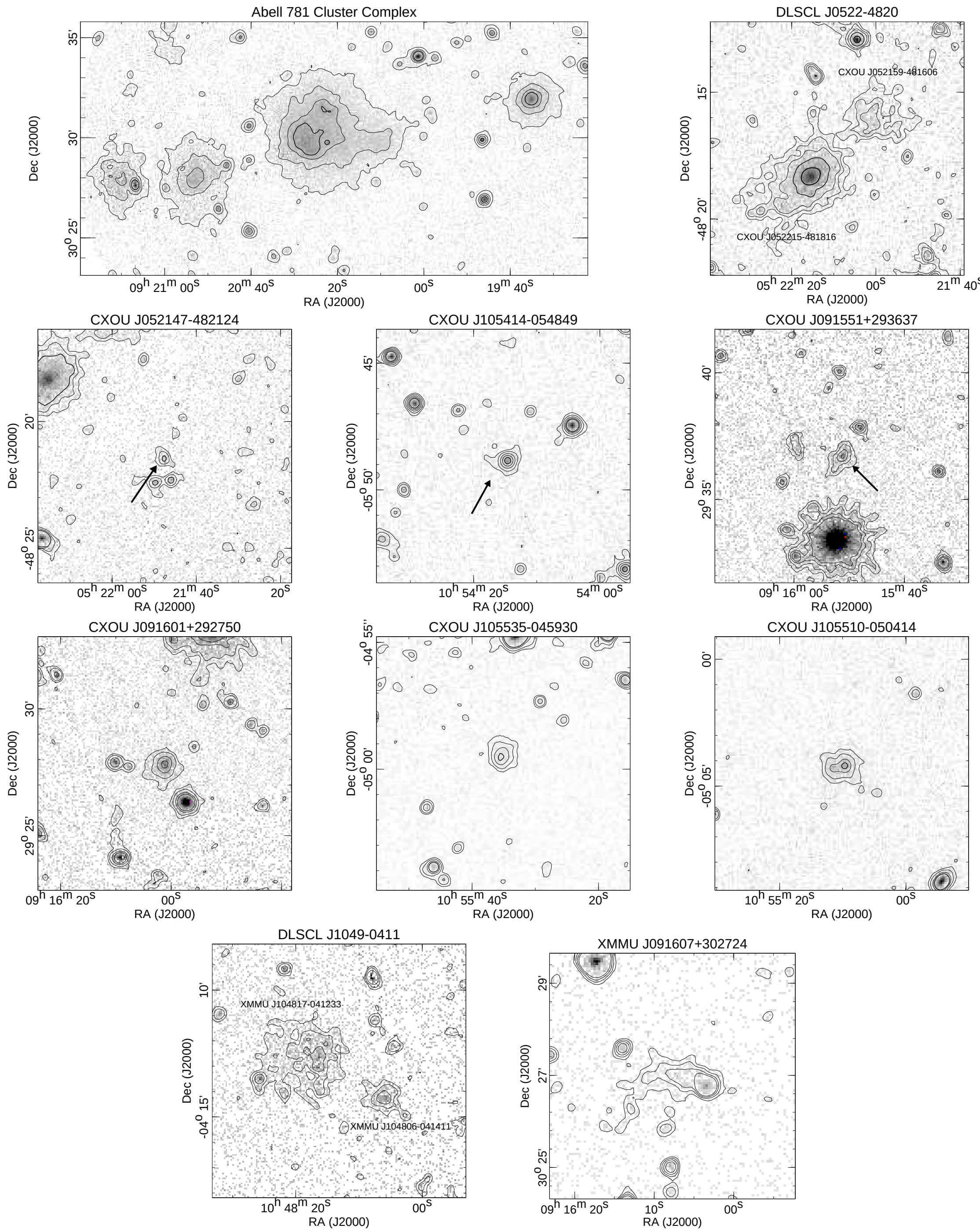

Figure 2.2 Significant X-ray clusters (indicated by arrows in some images) associated with DLS shear peaks. CXOU J105510-050414 and XMMU J091607+302724 have point sources within the cluster emission. The prominent object imaged with CXOU J091551+293637, is the point source that confuses emission of the central counterpart to DLSCL J0916.0+2931).

the DLS is less clear. A bright, extended, elliptical galaxy rests close to the X-ray position, and is a good candidate for the BCG. The X-rays fit well to the emission model of a cluster at the photometric redshift of this galaxy, $z_{ph} = 0.3$. There are few associated galaxies however, and so without more members, spectroscopy would be required to confidently associate this X-ray cluster with either its neighboring cluster (the nearby cluster above). So we do not confidently associate this cluster with the shear peak.

The remaining *beyond* subset shear peaks have been previously reported in the literature as weak lensing detections. DLSCL J0921.4+3013 was reported in the weak lensing reconstruction of DLS field F2 performed by Kubo et al. (2009). It does not appear, however, in the recent weak lensing analysis of Subaru Hyper Suprime-Cam (HSC) observations of F2, conducted by Miyazaki et al. (2015). The *XMM−PPS* finds three extended X-ray sources in this vicinity: two toward the north (B10a and B10b, Table 2.2) and one toward the south (B10c, Table 2.2).

The southern X-ray source, XMMU J092102+300530, is approximately $\sim 8'$ to the southeast of the DLS position and has no other weak lensing peak nearby. Thus, we cannot associate this X-ray source to a DLS shear peak. There is no corresponding cluster in the optical cluster catalog from the DLS (Ascaso et al. 2014) due to their bright star mask; however, visual inspection of the DLS images shows clear evidence for an optical cluster beyond the offending star. We estimate a photometric redshift ($z = 0.53$) from the galaxies in the cluster outskirts. The X-rays also fit nicely to a thermal cluster emission model at this redshift.

The two northern X-ray detections, B10a and B10b, lie closer to the DLS position ($\sim 3.5'$ away). They are small, $\lesssim 1'$ sized clumps, which overlie a much broader region of red galaxies in the DLS at similar redshifts ($z \sim 0.6$). Ascaso et al. (2014) report an optical cluster between the X-ray clumps at a redshift between $0.54 < z < 0.6$. The X-ray clumps do not have well defined peaks or shapes, and are difficult to associate with

Table 2.3 *XMM Newton* spectral fitting results: temperature and luminosity

	Name	X_ID	$\chi^2/$ *d.o.f.*	nH (LAB) 10^{20}cm^{-2}	z	Abund. $Z_\odot$	kT_X keV	L_X *Bolometric* 10^{44} ergs s^{-1}
1.	DLSCL J0920.1+3029	CXOU J092026+302938	2580/1881	1.65	0.302	$0.21^{+0.02}_{-0.02}$	$6.33^{+0.13}_{-0.13}$	$10.55^{+0.07}_{-0.07}$
		CXOU J092053+302800	1071/964	1.65	0.291	$0.21^{+0.05}_{-0.05}$	$3.19^{+0.13}_{-0.13}$	$2.08^{+0.06}_{-0.06}$
		CXOU J092110+302751	659/494	1.65	0.427	0.3	$3.87^{+0.41}_{-0.33}$	$2.67^{+0.07}_{-0.07}$
		XMMU J091935+303155	833/768	1.66	$0.428^{(a)}$	0.3	$3.41^{+0.15}_{-0.15}$	$3.30^{+0.05}_{-0.05}$
2.	DLSCL J0522.2−4820	CXOU J052215−481816	249/286	2.85	0.296	0.3	$4.03^{+0.25}_{-0.24}$	$3.67^{+0.06}_{-0.06}$
		CXOU J052159−481606	19/22	2.82	0.296	0.3	$4.34^{+1.31}_{-0.87}$	$0.84^{+0.05}_{-0.05}$
		CXOU J052147−482124	3/5	2.79	0.296	0.3	$1.05^{+0.44}_{-0.31}$	$0.05^{+0.02}_{-0.01}$
		CXOU J052246−481804$^{\Delta}$	11/11	2.91	0.210	0.3	$1.48^{+0.44}_{-0.21}$	$0.07^{+0.01}_{-0.01}$
4.	DLSCL J1054.1−0549	CXOU J105414−054849	79/63	2.43	0.190	0.3	$1.07^{+0.03}_{-0.04}$	$0.06^{+0.003}_{-0.003}$
7.	DLSCL J0916.0+2931	CXOU J091551+293637	17/15	1.72	0.530	0.3	$1.44^{+0.22}_{-0.16}$	$0.58^{+0.10}_{-0.10}$
		CXOU J091601+292750	62/55	1.74	0.531	0.3	$2.09^{+0.19}_{-0.19}$	$1.01^{+0.07}_{-0.07}$
8.	DLSCL J1055.2−0503	CXOU J105535−045930	36/38	2.40	0.609	0.3	$3.38^{+0.46}_{-0.44}$	$1.04^{+0.07}_{-0.06}$
		CXOU J105510−050414	33/32	2.39	0.680	0.3	$4.14^{+0.69}_{-0.57}$	$2.80^{+0.17}_{-0.17}$
Beyond the initial Wittman et al. (2006) publication:								
B9.	DLSCL J1048.5−0411	XMMU J104817−041233	38/40	3.69	$0.246^{(b)}$	0.3	$2.38^{+0.36}_{-0.29}$	$0.55^{+0.03}_{-0.03}$
		XMMU J104806−041411$^{\Delta}$	8/9	3.69	$0.30^{(c)}$	0.3	$1.64^{+0.44}_{-0.27}$	$0.17^{+0.02}_{-0.02}$
B10.	DLSCL J0921.4+3013	XMMU J092102+300530$^{\Delta}$	13/13	1.65	$0.53^{(c)}$	0.3	$2.08^{+0.65}_{-0.43}$	$0.56^{+0.06}_{-0.06}$
B11.	DLSCL J0916.3+3025	XMMU J091607+302724	16/20	1.10	$0.650^{(d)}$	0.3	$5^{\dagger}$	$1.35^{+0.14}_{-0.14}$

NOTE:− In the column heading kT_X, k is the Boltzmann constant.
Redshift sources:
$^{(a)}$ Sehgal et al. (2008), $^{(b)}$ this work − spectroscopy (§2.2.2), $^{(c)}$ this work − DLS photometry (§2.2.2), and
$^{(d)}$ Geller et al. (2014).
$^{\Delta}$X-ray cluster not confidently associated to shear peak.
† Temperature fixed at nominal value; data could not constrain.

the galaxies as independent clusters or as a single cluster with poor X-ray emission. We find these data to be consistent with the interpretation presented in Starikova et al. (2014) as a superposition of low mass systems. Furthermore, the detection significance for the X-ray sources (XMMU J092124+301324 and XMMU J092118+301156) using nominal regions (see Table 2.2) is low and so we do no further spectral analyses on them. Because these two are too faint, and the southern cluster (B10c) is too far away, we cannot report properties of associated X-ray clusters for DLSCL J0921.4+3013.

The third shear peak in the *beyond* subset, DLSCL J0916.3+3025, was not found in the weak lensing analysis of Kubo et al. (2009). More recently, two weak lensing detections near this position have been reported. Utsumi et al. (2014), in their analysis of a Subaru Suprime camera observation of a part of the DLS field F2, and Miyazaki et al. (2015), in their weak lensing analysis of a Subaru Hyper Suprime-Cam (HSC) observation covering all of the same DLS field, both find weak lensing detections that are within $\sim 1'$ (but on opposite sides) of the corresponding X-ray source position (of B11). A nearby optical cluster ($z \sim 0.54$, Ascaso et al. 2014) is found to be approximately $\sim 1.5'$ away from the X-ray source and possibly consistent with the Miyazaki et al. (2015) weak lensing peak. We make a plausible association between the X-ray source and the Miyazaki/Utsumi detections. The X-rays are faint and do fit to a thermal cluster emission model, but with the temperature fixed at a nominal value. We describe next our steps to extract spectra and fit them to measure luminosities and temperatures.

2.2.3 Extracting Spectra

We generated X-ray spectra from newly calibrated event-lists; these are among the outputs of the *XMM-PPS* run performed above (§2.2.2), on the raw data with updated calibration files. We use the *XMM-Newton Science Analysis System* (*XMM-SAS*) software package to run this pipeline and to process this data further. The newly calibrated event lists from each camera were filtered in time to remove periods of highly flaring soft proton background. The resulting exposures are listed in Table 2.1. Spectra and other products necessary for spectral fitting were generated with these flare-filtered data.

Spectra were extracted from within regions that we defined on our soft-band images. These same regions were also used to determine the detection properties and are listed alongside in Table 2.2. We began the region selection by drawing contours on our $0.5 - 2.0$ keV images, at levels of count rate per pixel that are 1.5 times the background level and higher. The outermost contour guided our initial choice of either circular or elliptical source region, which was placed to just surround the contour. We refined the size of this region by 5 or 10 percent iteratively until the luminosity measured from within converged. In this way, we were sure to have collected all of the cluster emission with minimal contamination from the unresolved X-ray background.

Resolved background sources, found either by *XMM-PPS* or present obviously in available *Chandra* images, were excluded. Background regions were placed as annuli around source regions, and also excluded any *XMM-PPS* detected point sources or neighboring cluster regions.

Spectra and other data products used in fitting (arfs and rmfs) were generated with the standard binnings, event filters, and other recommended parameters suggested by the *XMM Newton* team for analyzing extended X-ray sources. Among these recommendations, we chose to weight the response files by the cluster images to better account for brightness variations.

2.2.4 Measure X-ray Temperature & Luminosity

X-ray spectra from regions described above (§2.2.3) were fit in `XSPEC` to a product of the `MeKaL` model (Mewe et al. 1985, 1986; Kaastra 1992) and the `phabs` model. The `MeKaL` model describes a thermal plasma with ionized atomic components, with model parameters describing gas temperature, abundance, redshift, and the emission measure (proportional to the fit normalization). The `phabs` model describes galactic photoelectric absorption and depends only on one parameter, the absorbing column density.

We generally let temperature and normalization vary, and fixed all remaining parameters. We fixed abundance to 0.3 [$Z_\odot$] except when data quality could support a constraint. The redshift was set to the spectroscopic value determined by the DLS (`W06`) or other follow up work (indicated in Table 2.3). If the data were too poor to constrain both temperature and normalization, we fixed the temperature to a reasonable value (see Table 2.3). In all cases, the column density for the `phabs` model was fixed to the galactic neutral hydrogen column densities measured by the Leiden/Argentine/Bonn (LAB) survey (Kalberla et al. 2005) at the cluster position.

All spectra of each cluster, one from each of the three cameras, were simultaneously fit to one function in `XSPEC`. Uncertainties due to poor subtraction of telescopic fluorescence lines were addressed independently for PN and MOS by excluding the affected channels. Background scaling was adjusted by examining the high energy [10 keV−12 keV] counts (Vikhlinin et al. 2009) where no source emission is expected. High energy channels, where emission from a given cluster was negligible, were excluded from the spectral fit. Below, I discuss some additional details of the analysis for individual clusters.

Analysis Notes on Individual Clusters

The notes that follow mention additional analysis details that vary per cluster, and so could not be included in the general analysis description above (§2.2.1-§2.2.4). The uninterested reader may skip to the next sub-section which describes the L_X, and T_X properties of our shear-selected X-ray clusters, and how they compare to other X-ray selected samples. Many DLS shear peaks have multiple X-ray counterparts in each *XMM Newton* observation, and some of them fall on chip gaps of the X-ray CCDs. We are thus unable to apply established methods to generating precise mass proxies (e.g. Vikhlinin et al. 2009). We make our best efforts to achieve convergence of temperature and luminosity measurements given the limitations in our observations. Below, we address these limitations for the affected clusters.

DLSCL J0522.2-4820

The spear peak DLSCL J0522.2-4820 is the second highest ranked in shear signal-to-noise. Its X-ray observation unfortunately has a large fraction of contaminated data from soft proton flares. We had to make very stringent cuts in the rate curves to remove the contaminated fraction and to avoid biasing cluster properties (see exposure after cuts in Table 2.1). We check our results against properties determined with the lower exposure *Chandra* data which originally confirmed the DLS clusters. We find good agreement, generally, between the two sets of X-ray properties (from *Chandra* and *XMM Newton* data) but find that two clusters warrant some discussion. These two are imaged in Figure 2.3, and are called here the “main” cluster (the larger of the two) and cluster “B” (the smaller).

The temperatures estimated for the main cluster from *Chandra* and *XMM Newton* are in statistical agreement, however the luminosities disagree with the *Chandra* data supporting a slightly lower estimate. This cluster is situated over chip gaps in both telescope detectors, and the information lost is not quite recoverable. The *Chandra* observation, shows the cluster centered on the gap in the middle of its field of view. The resulting loss of flux here cannot be accurately recovered as it would require a priori knowledge of the central brightness of the cluster (which is an attribute that varies from cluster to cluster, and does not always scale with the brightness distribution away from the cluster core. The *XMM Newton* observation also shows chip gaps (in all three cameras) passing through several parts of the cluster outskirts. The flux lost from the brighter center in the *Chandra* observation could be comparable to that lost from the many gaps in the dimmer cluster outskirts of the *XMM Newton* observation simply because there is much more of the cluster area that is in the *XMM*

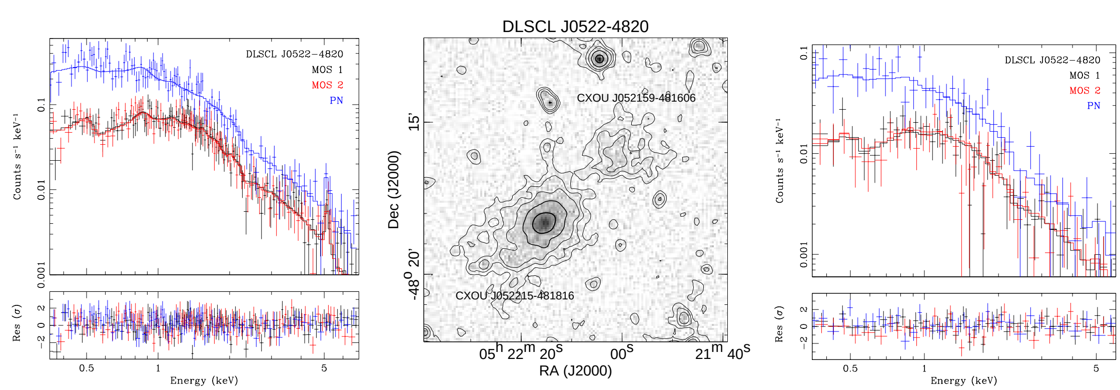

Figure 2.3 J0522-4820: Images and spectra of the main and the nearest to the main cluster. The spectrum on the left is for the main cluster.

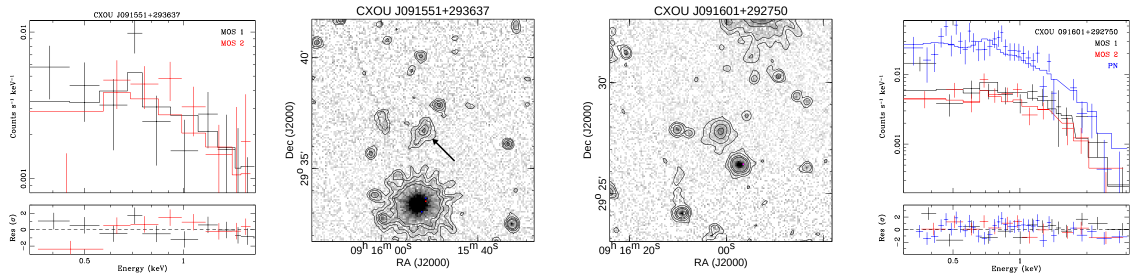

Figure 2.4 DLSCL J0916+2931: The northern X-ray counterpart and its spectrum are on the left, indicated by the arrow, and the southern is on on the right. The more prominent source in the images is a known BL lac object.

Newton chip gaps than in the *Chandra* gap. One can typically attempt an estimate of the flux lost in the gaps in the outskirts by estimating an average exposure for the gap region to scale the flux from neighboring regions appropriately (including the gap area), however, such an estimate becomes less useful for complicated gap distribution and geometry (e.g., where gaps intersect), and for asymmetric cluster emission as is the case for this cluster. We conclude that both luminosity estimates are lower limits that are still close to the true values. The pair of T_X, and L_X values we derive are in accord with the luminosity-temperature relation (see §2.2.6).

The case of cluster B is the discrepant one with neither estimates of temperature or luminosity agreeing from the *Chandra* and *XMM Newton* analyses. This disagreement may result from the PN chip gap that passes through the center of the cluster. The *Chandra* image of this cluster is entirely free of chip defects and shows a nice peak in the center which is missing from the three camera *XMM Newton* image (Figure 2.3). Missing emission from the center of the cluster could bias the spectrum toward higher temperatures, resulting in the higher *XMM Newton* value compared to *Chandra*.

DLSCL J0916.0+2931

The northern X-ray counterpart to DLSCL J0916+2931 are imaged in Figure 2.4. This cluster, CXOU J091551+293637, overlies chip gaps in all three *XMM Newton* cameras. The MOS gaps are in the outskirts of the cluster, but the PN gap coincides with the center of the cluster. The missing PN data has a strong effect in the image, which clearly shows a directional dip in the surface brightness distribution along the gap, making for overall odd-shaped contours. The resulting PN spectrum is very noisy, and its count-rate measurement is low by comparison. We thus exclude the PN data from our analysis. To compensate for the gaps in the MOS data, we scale the MOS1 and MOS2 spectral norms independently during fitting, and report the brighter of the two luminosities. The spectra are well behaved, and plotted in Figure 2.4 and the resulting temperature and the luminosity are tabulated in Table 2.3.

The southern X-ray cluster, CXOU J091601+292750, was imaged over few to no compromising chip gaps in the three cameras. Read-out associated issues, however, such as offset columns, have rendered this cluster's data a prime example for the case of adjusting background scaling. Background area was scaled until the high energy count rates, where no cluster emission is expected, were reduced to zero. After this correction, the spectra from all three cameras fit independently, resulted in statistically consistent luminosities and temperatures. The image and spectra for this cluster are shown in Figure 2.4.

DLSCL J1055.2−0503

Both X-ray counterparts of DLSCL J1055.2-0503 are imaged in Figure 2.5 . The southern X-ray source, CXOU J105510−050414, is positioned well on both MOS cameras with no chip gaps within the source region. The PN observation, however,

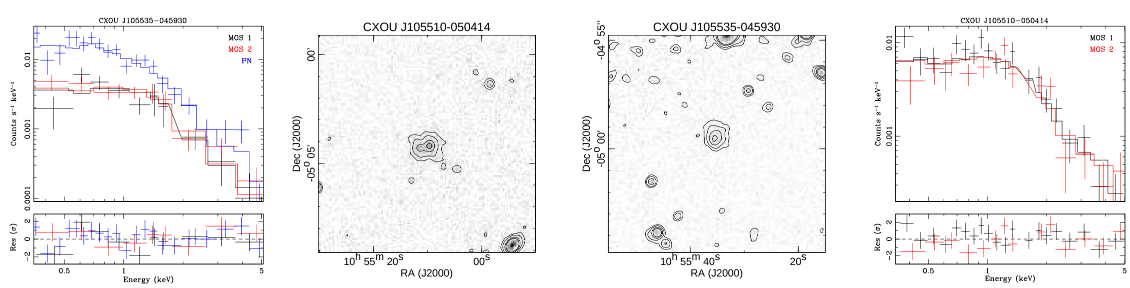

Figure 2.5 DLSCL J1055-0503

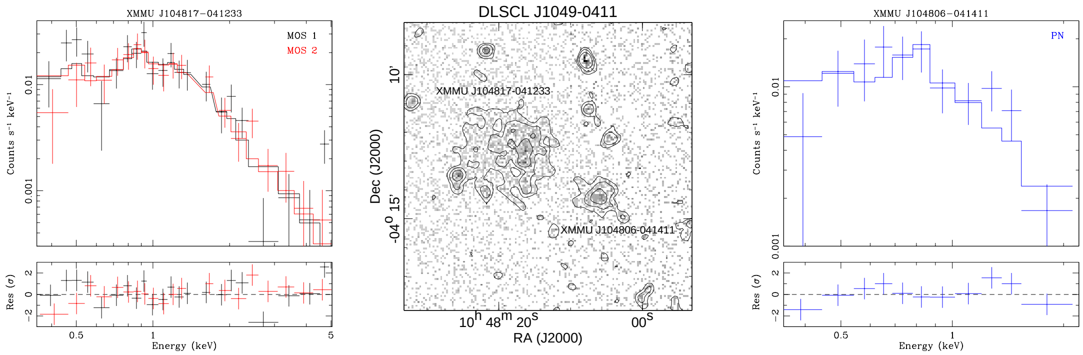

Figure 2.6 DLSCL 10485-0411: Main X-ray counterpart is the larger of the sources in the image, and its spectrum is to the left.

basically misses the center of the cluster with a chip gap. There is a point source, confirmed with *Chandra* imaging, located 19.5″ from the X-ray peak, which ends up dominating the emission in the PN observation because of the missing cluster emission. We thus ignore the PN data for this analysis and remove the point source with a 12″ region from MOS observations.

The southern source, CXOU J105510–050414, is positioned well on both MOS cameras toward a side of the central chip. No gaps are present within the source region. The PN observation, on the other hand, essentially masks the cluster center with a chip gap. There is a point source, confirmed by *Chandra* located 19.5″ from the cluster, which ends up dominating the emission in the PN observation. We thus ignore PN data for this analysis and remove the point source with a 12″ region from MOS observations. The point source region size was chosen to include as much cluster emission as possible without affecting the measured temperature. The resulting fit is good with a $\chi^2/d.o.f$ of 33/32.

DLSCL 1048.5−0411

DLSCL 10485−0411 of the beyond sample is imaged in Figure 2.6 which shows the main X-ray counterpart as well as the additional X-ray source which cannot be definitively associated with the shear peak (§2.2.2). The main cluster, XMMU

J104817−041233 is yet another case of a PN chip gap cutting through X-ray peak (which is obviously present in the MOS data). Since there are no *Chandra* observations of the *beyond* sample, there is no additional scope for comparison of X-ray properties. We exclude the PN data from this analysis as well. The MOS data are not compromised by chip gaps or other features and fit well to a single temperature `MeKaL` model. Resulting properties are reported in Table 2.3.

The secondary X-ray source, XMMU J104806-041411, is located to the southwest of the main X-ray cluster and is observed well by the PN camera. On the MOS cameras however, this clusters sits on the corners of the central chips and their associated gaps pass $\sim 20''$ from the peak, which results in a significant loss of flux. We choose to exclude all MOS data to avoid biasing temperature and luminosity incorrectly and get a good fit to the PN data alone with a $\chi^2/d.o.f$ of 8/9. As a test, when we include the MOS data and allow temperature (and normalization) to vary relatively between the cameras, we indeed see a much poorer fit with $\chi^2/d.o.f$ of 19/13 to a biased temperature and lower luminosity.

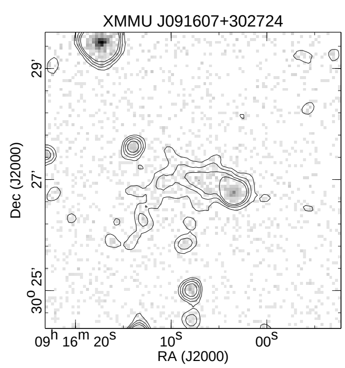

Figure 2.7 DLSCL J0916+3025: The image is roughly centered on peak of the extended emission, and shows the brighter point source to the west. The point source emission is confused with some of the cluster emission causing the contours to broaden to the west.

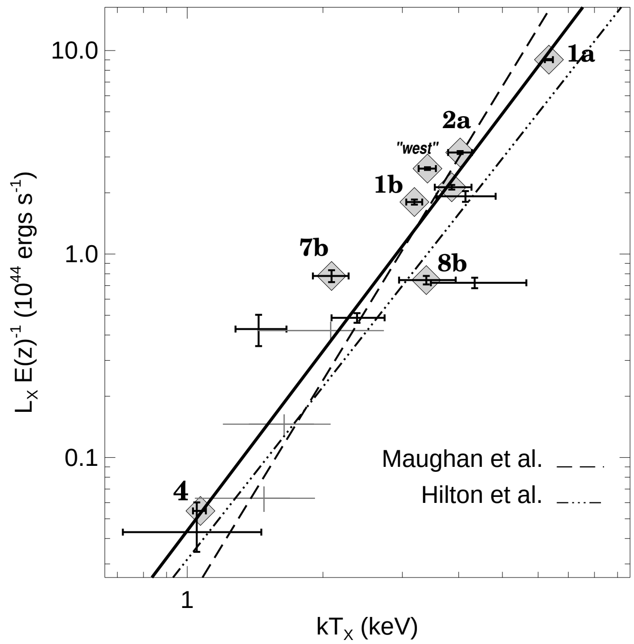

Figure 2.8 Temperatures and bolometric luminosities from Table 2.3. Solid line is the fit to our data. Filled diamonds mark clusters with both X-ray and weak lensing masses and are given labels from Table 2.4. The un-labeled diamond point is cluster 1c. Grey points were not included in the fit; these are clusters that we were unable to confidently associate with DLS shear peaks (§2.2.2).

DLSCL J0916.3+3025

The observation of XMMU J091607+302724 is of insufficient quality to constrain both a temperature and luminosity, however there is clear evidence for diffuse emission. Fig. 2.7 shows the faint extended emission of the cluster next to the bright dominating point source ($\sim 65''$ away). The data is further compromised by two PN chip gaps crossing through the peak of the extended emission. The quality of the best spectrum is too poor to constrain both temperature and luminosity. We can, however, fix the temperature of this source and estimate a luminosity (see Table 2.3). Given the high redshift of the source, a reasonable choice for the temperature is 5 keV. In a slightly different X-ray analysis, Starikova et al. (2014) who have this cluster in common with our sample, find a $\sim 3\sigma$ temperature measurement of 4.6 keV. The measured soft-band (0.5-2.0 keV) flux for this cluster is indeed low at a value of 2.64×10^{-14} erg s^{-1} cm^{-2}.

2.2.5 The resulting L_X, T_X of sample.

The resulting temperatures and bolometric luminosities from these fits, for 14 X-ray clusters associated with DLS shear peaks, and three serendipitous X-ray clusters, are shown in Table 2.3, along with the corresponding model parameters. Temperatures and luminosities are also plotted in Figure 2.8, where the luminosities corrected for expansion (i.e., $\times E(z)^{-1}$). Previously determined properties for some of these clusters (Starikova et al. 2014) are consistent with the values we determine. The ranges of these properties are broad, spanning over four orders of magnitude in luminosity and a factor of six in temperature.

The luminosity range includes the order of the brightest known clusters (10^{45} erg s^{-1}), as well as that of small groups ($10^{41} - 10^{42}$ erg s^{-1}). The temperature range does not reach very high, but includes the average hot cluster ($\gtrsim$ 5 keV) as well as many low group-like values ($\sim$ 1keV). Morphology is difficult to quantify for the whole sample due to some clusters with poor statistics, but a visual examination of the sample (see Fig. 2.2) reveals a full range from smooth and highly centrally peaked to generally disturbed and lumpy. The disturbed morphology seems to be associated with both interacting systems (see §2.3.1), and isolated ones. To understand these sample properties in the context of other well-understood X-ray clusters we make a comparison of the luminosities and temperatures as well as of the $L_X - T_X$ relation to X-ray selected samples from the literature.

We choose literary comparison samples that are selected in the X-ray, and that have luminosities and temperatures determined without excising cores, as we do. Two such samples, with comparable redshift, temperature and luminosity ranges, are presented by Maughan et al. (2012), and Hilton et al. (2012), hereafter called M12 and H12. We find that the general distribution of cluster morphology is also consistent with those of the M12 and H12 samples. We discuss our $L_X - T_X$ relation, and its comparison to the relations derived in H12 and M12 samples next.

2.2.6 The $L_X - T_X$ relation

The luminosity-temperature relation of typical X-ray clusters is a tight correlation, born out of the cluster growth process (e.g., Kaiser 1986; Vikhlinin et al. 2009). Historically, it has distinguished samples that deviate from self-similarity (e.g., Markevitch 1998; Arnaud & Evrard 1999). More recent studies have shown the slope of this relation to vary with measures of dynamical activity in clusters (M12; Mahdavi et al. 2013). Clusters selected without regard to dynamical state tend to show higher slopes (> 3) (e.g., Mantz et al. 2010; Hilton et al. 2012), as also do smaller galaxy groups (e.g., Sun et al. 2009). On the other hand, carefully selected samples of relaxed clusters, with core-removed temperatures (e.g., M12), produce $L_X - T_X$ relations closer to the expected self-similar relation ($L \sim T^2$). Selection effects also affect the slope, such as e.g., Malmquist bias, which tends to lower the slope. We determine the luminosity-temperature relation of our shear-selected sample to see how the clusters scatter around the best fit relation, and to compare its best fit relation to X-ray selected cluster samples.

The mathematical form of the relation to which we fit our L_X, T_X data is, $h(z)^{-1}L_{X,bol} = L_0\,(T_X/5.0keV)^{\alpha}$. The data were fit by performing a linear regression on the logarithm of the luminosities and temperatures. We use the orthogonal `BCES` method (Akritas & Bershady 1996) for the regression, after symmetrizing our errors in temperature. Our best fit is shown in Figure 2.8 by the solid line; it has a log space slope of $\alpha = 2.93 \pm 0.15$ and an intercept of $\log(L_0/1 \text{ erg s}^{-1}) = 44.69 \pm 0.08$. X-ray clusters that could not be associated with shear peaks (noted in Table 2.3) were not included in the fit, but are shown on the plot as unmarked grey error bars.

First we note that our $L_X - T_X$ relation is not consistent with the self-similar slope ($\alpha = 2$). The L_X, T_X points scatter tightly around the comparison relations as well as the best fit plotted in Figure 2.8. The M12 relation (dashed line) is from their full sample of 114 clusters selected without regard to dynamical state. Their slope of $\alpha = 3.63$ is slightly steeper than ours, although still consistent at $<2\sigma$. The H12 relation (dash-triple dotted line) is from their intermediate redshift ($0.25 < z < 0.5$) sample of 77 clusters also selected without regard to dynamical state; it has a slightly shallower slope than ours at $\alpha = 2.82$. Both of these relations for X-ray selected samples are consistent with our clusters selected in weak lensing. This result is also consistent with and confirms a similar finding by Giles et al. (2015), who fit nine shear-selected X-ray clusters to an $L_X - T_X$ relation of similar form and get a slope and normalization $\alpha = 2.63 \pm 0.69$ and $\log(L_0/1 \text{ erg s}^{-1}) = 44.44 \pm 0.15$ (we have converted their normalization to one that would match a pivot-temperature of 5 keV).

2.3 Mass Estimates & Comparison

Along with studying X-ray properties (L_X,T_X, & M_X) of weak lensing selected clusters, we do a direct comparison of mass estimates between weak lensing and X-ray. For the weak lensing mass estimates, we take the values obtained in Abate et al. (2009). Our X-ray data are not of sufficient depth to estimate hydrostatic masses, however, they do allow X-ray temperature to be used as a mass proxy for a fraction of the sample. X-ray temperature correlates more tightly with the mass (e.g., Vikhlinin et al. 2009), and so we choose this over the luminosity as the proxy. We are unable to determine surface brightness profiles for most of the X-ray clusters so mass proxies such as the gas mass fraction, f_g, and the integrated gas mass times the temperature, Y_X, cannot be used.

2.3.1 X−ray Mass Estimates

We consider two $M_X - T_X$ relations to start, and proceed with two sets of X-ray mass estimates. One relation is derived from *XMM Newton* data by Arnaud et al. (2005), and the other is derived from *Chandra* data by Vikhlinin et al. (2009). Our aim here is to study any variation that may arise in our mass estimates from the choice of $M_X - T_X$ relation and to compare to published mass estimates when available. The temperature measurement requires that the central core emission be removed, which means that we are able to get mass estimates for only nine X-ray clusters.

Both $M_X - T_X$ relations use masses within a fixed overdensity of Δ=500 times the critical density, $\rho_{cr} = \frac{3H^2}{8\pi G}$. To obtain our own values of R_{500}, we employ an iterative procedure. We start with a temperature from Table 2.3, and estimate a mass from the $M_X - T_X$ relation. This mass then gives an R_{500} via, $R_\Delta = \left(M_{tot}\left(T_X\right) / \left(\Delta \frac{4\pi}{3}\rho_{cr}\right)\right)^{1/3}$. Using this R_{500} we extract a new spectrum, excluding the core emission inside r_i. The inner and outer radii for extraction for the Arnaud et al. and Vikhlinin et al. relations are r_i–$r_o = 0.1R_{200} - 0.5R_{200}$ and r_i–$r_o = 0.15R_{500} - R_{500}$ respectively. The newly extracted spectrum gives a temperature inside the correct overdensity radius and produces the first estimates of M_{500} and R_{500}. Uncertainties in these are the result of propagating statistical measurement uncertainties of the spectral fit parameters as well as the uncertainties in the relation coefficients. We repeat this process until subsequent M_{500} and R_{500} values converge to within measured uncertainty. Data quality limits our ability to carry out this procedure for all clusters, and in Table 2.4 we report the masses for the nine clusters for which this was possible.

The two sets of X-ray masses from the two different scaling laws agree well for the majority of the sample, but diverge at high temperatures (see Figure 2.9). As it turns out, the differently prescribed extraction radii for measuring core-excised temperatures for the two different scaling laws, roughly correspond to similar values

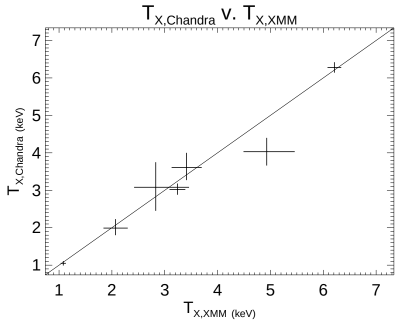

$kT_{X,ce}$ keV		M_{500} $10^{14} M_{\odot}$	
(a)	(v)	(a)	(v)
$6.21^{+0.13}_{-0.13}$	$6.28^{+0.14}_{-0.14}$	$6.81^{+0.25}_{-0.25}$	$5.17^{+0.21}_{-0.21}$
$3.24^{+0.15}_{-0.15}$	$3.02^{+0.16}_{-0.14}$	$2.25^{+0.18}_{-0.18}$	$1.72^{+0.14}_{-0.12}$
$3.41^{+0.29}_{-0.28}$	$3.61^{+0.39}_{-0.34}$	$2.28^{+0.34}_{-0.32}$	$2.09^{+0.36}_{-0.29}$
$3.64^{+0.29}_{-0.19}$	$3.24^{+0.20}_{-0.19}$	$2.54^{+0.35}_{-0.23}$	$1.77^{+0.16}_{-0.16}$
$4.93^{+0.53}_{-0.44}$	$4.03^{+0.37}_{-0.37}$	$4.60^{+0.89}_{-0.67}$	$2.67^{+0.39}_{-0.36}$
$1.08^{+0.05}_{-0.05}$	$1.05^{+0.06}_{-0.06}$	$0.37^{+0.03}_{-0.03}$	$0.36^{+0.04}_{-0.04}$
$2.07^{+0.23}_{-0.23}$	$1.99^{+0.24}_{-0.19}$	$0.91^{+0.18}_{-0.17}$	$0.80^{+0.15}_{-0.12}$
$2.83^{+0.63}_{-0.41}$	$3.08^{+0.67}_{-0.63}$	$1.49^{+0.61}_{-0.36}$	$1.47^{+0.51}_{-0.44}$

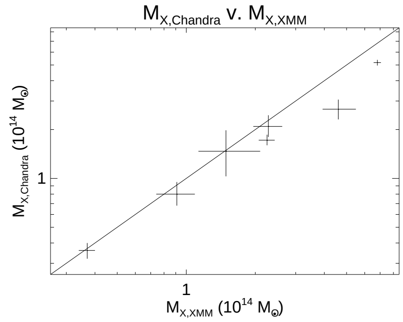

Figure 2.9 Temperature and mass comparisons between *Chandra* and *XMM Newton* data based M-T laws. Temperature estimates from *Chandra* and *XMM Newton* data agree very well, but mass estimates diverge at high temperature. Solid line in plots is unity. A $^{(v)}$ marks column of parameters resulting from iteration with the Vikhlinin et al. (2009) M-T law. An $^{(a)}$ marks column of parameters resulting from iteration with the Arnaud et al. (2005) M-T law.

in the angular scale, and so it is not surprising that the resulting values of core-excised temperatures from each set of iterations per cluster are statistically consistent. Given the comparable temperatures, the divergence in mass estimates must arise from differences in the scaling laws themselves.

To discriminate between these estimates, and following the tradition of calibrating scaling laws, we compare to the hydrostatic masses determined by Sehgal et al. (2008) which use both *Chandra* and *XMM Newton* data. We find that their hydrostatic masses agree with our estimates based on the Vikhlinin et al. (2009) relation. Since our remaining mass estimates agree, we report one set of X-ray masses in Table 2.4, determined using the Vikhlinin et al. (2009) relation. Table 2.4 also presents the new core-excised temperature and R_{500} estimates along with goodness of fit indicators. We include more exposure than the Sehgal et al. (2008) observation so our statistical uncertainties on the measured temperatures are smaller. Our choice to present masses from the Vikhlinin et al. (2009) relation does not affect any conclusions we draw regarding the X-ray and weak lensing mass comparison.

Table 2.4 R_{500}, T_{500}, & M_{500}

	Name	X_ID	χ^2/ *d.o.f.*	R_{500} $'$ (kpc)	$kT_{X,500}$ keV	M_{500} $10^{14}M_\odot$	M_{WL} $10^{14}M_\odot$
1.	DLSCL J0920.1+3029	^{1a} CXOU J092026+302938	1641/1526	$4.11 \pm 0.05(1103 \pm 15)$	$6.28^{+0.14}_{-0.14}$	$5.17^{+0.21}_{-0.21}$	$3.39^{+0.18}_{-0.18}$
		^{1b} CXOU J092053+302800	1071/964	$2.93 \pm 0.08(768 \pm 20)$	$3.02^{+0.16}_{-0.14}$	$1.72^{+0.14}_{-0.12}$	$2.91^{+0.57}_{-0.38}$
		^{1c} CXOU J092110+302751	659/494	$2.30 \pm 0.13(772 \pm 45)$	$3.61^{+0.39}_{-0.34}$	$2.09^{+0.36}_{-0.29}$	$1.94^{+0.66}_{-0.57}$
		^{west}XMMU J091935+303155	833/768	$2.23 \pm 0.05(745 \pm 16)$	$3.24^{+0.20}_{-0.19}$	$1.77^{+0.16}_{-0.16}$	$1.8^{+1.0(a)}_{-0.6}$
2.	DLSCL J0522.2−4820	^{2a} CXOU J052215−481816	144/152	$3.34 \pm 0.09(1020 \pm 23)$	$4.03^{+0.37}_{-0.37}$	$2.67^{+0.39}_{-0.36}$	$0.99^{+0.20}_{-0.39}$
4.	DLSCL J1054.1−0549	CXOU J105414−054849	79/63	$2.50 \pm 0.10(475 \pm 19)$	$1.05^{+0.06}_{-0.06}$	$0.36^{+0.04}_{-0.04}$	$0.40^{+0.20}_{-0.20}$
7.	DLSCL J0916.0+2931	^{7b} CXOU J091601+292750	74/67	$1.43 \pm 0.08(540 \pm 32)$	$1.99^{+0.24}_{-0.19}$	$0.80^{+0.15}_{-0.12}$	$0.10^{+0.30}_{-0.00}$
8.	DLSCL J1055.2−0503	^{8b} CXOU J105535−045930	22/17	$1.59 \pm 0.17(641 \pm 68)$	$3.08^{+0.67}_{-0.63}$	$1.47^{+0.51}_{-0.44}$	$2.30^{+0.84}_{-0.84}$
Beyond the initial Wittman et al. (2006) publication:							
B9.	DLSCL J1048.5−0411	XMMU J104817−041233	25/23	$3.13 \pm 0.31(728 \pm 72)$	$2.41^{+0.57}_{-0.42}$	$1.41^{+0.19}_{-0.46}$	...

NOTE:− Superscripts to the left of the X-ray IDs are identifiers given by A09, re-introduced here for easy reference within the mass comparison plot in Fig. 2.10. The ^{west} label refers to the Abell 781 "west" cluster, using the naming convention from Sehgal et al. (2008). The $^{(a)}$ indicates this mass is obtained from Wittman et al. (2014) (see §2.3.3).

2.3.2 Weak Lensing Mass Estimates

For all X-ray counterparts of the DLS shear peaks published in 2006, Abate et al. (2009), hereafter A09, obtained weak lensing mass estimates. We briefly summarize their key steps here. For each X-ray cluster, A09 fit a mass distribution model based on the NFW mass density profile to its observed two dimensional shear profile. Shear profiles were measured from source galaxy ellipticities, considering their full three dimensional positions (using photometric redshifts). Centers of these profiles were fixed to positions of the X-ray peaks within a Gaussian window of 81 kpc (reported in table 1 of A09).

Where applicable, shear profiles were fit simultaneously for multiple neighboring X-ray clumps, by adding shear linearly. The simultaneous fits account for the influence of neighboring mass concentrations on the shear of a given cluster and are thus believed to be more accurate than fitting each cluster individually. Their resulting masses are integrated out to an overdensity radius of Δ=200 (table 3, A09), which we convert to masses within an overdensity radius of Δ=500 assuming an NFW mass density profile and the observed mass concentration relations in Duffy et al. (2008). We list these masses in the last column of Table 2.4 for the seven clusters we use from A09.

We additionally include one weak lensing mass from Wittman et al. (2014) because it was not in the A09 study. Wittman et al. (2014) perform a similar analysis fitting multiple shear profiles simultaneously, with centers guided by the X-ray peaks. The mass model is also based on the NFW profile, and their fitting additionally incorporates a tomographic weighting.

2.3.3 X-ray – Weak Lensing Mass Comparison

We thus have a set of 8 clusters with both X-ray and weak lensing mass estimates for comparison. These eight clusters cover the full ranges of weak lensing masses, X-ray temperatures (e.g., T_X Table 2.3), and redshifts of the full sample.

We plot the weak lensing and X-ray M_{500} values against each other in Figure 2.10. Some individual clusters discussed below are marked in this figure with identifiers listed in Table 2.4. The two sets of mass estimates are broadly consistent with each other, scattering on either side of equality. The scatter about equality is large and there are two statistical outliers in the plot. We discuss the agreement, both overall and individually, between the weak lensing and X-ray masses in detail below, beginning with some noteworthy cases.

Notes on Individual Comparisons

The only shear peak in our sample (rank 4) which has just one corresponding X-ray cluster, CXOU J105414 − 054849, shows the best agreement in mass. The X-ray and shear-estimated masses for this cluster are in excellent agreement with $M_{500}^{WL} = 0.40 \pm 0.2 \times 10^{14} M_\odot$ and $M_{500}^{X\text{-}ray} = 0.36 \pm 0.04 \times 10^{14} M_\odot$. The prominent case in our sample of shear resulting from superposed clusters (at different redshifts), Abell 781, presents with comparable masses when summed across the multiple components. The three components with A09 masses add to $\sum M_{500}^{WL} = 8.24 \pm 0.80 \times 10^{14} M_\odot$, with uncertainties crudely added in quadrature. The corresponding sum of X-ray masses

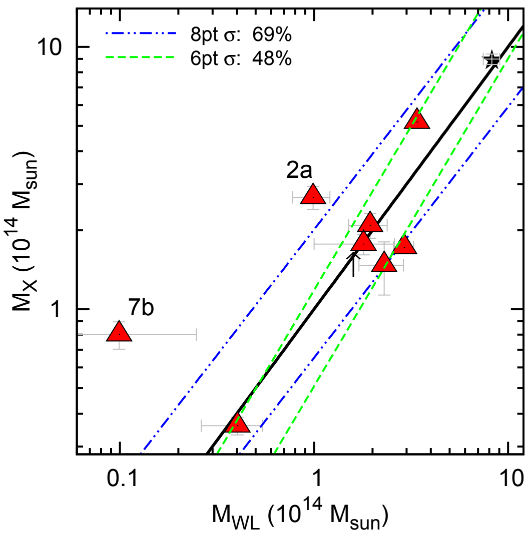

Figure 2.10 The solid line shows equality. Intrinsic scatters determined including (8pt) and excluding (6pt) the outliers (§2.3.3) are plotted in the dash-dotted patterns; the corresponding best fit lines (not shown) are exactly in between the lines of scatter. Labels refer to cluster IDs in Table 2.4. The star is the summed mass of Abell 781 (§2.3.3); its west cluster is marked with an arrow.

is indeed crudely comparable at $\sum M_{500}^{X\text{-}ray} = 8.98 \pm 0.41 \times 10^{14} M_\odot$ (see star point on mass comparison plot in Figure 2.10).

The X-ray mass we obtain for XMMU J091935+303155, the "West" cluster in the Abell 781 complex, does not have a corresponding weak lensing mass in Abate et al. (2009). It does however have a weak lensing mass measurement in Wittman et al. (2014), and we use this value, $M_{500}^{WL} = 1.8^{+1.0}_{-0.6} \times 10^{14} M_\odot$, in the sample mass comparison section below. The mass comparison of this cluster has been the subject of some controversy in the literature. Cook & Dell'Antonio (2012) claimed that the weak lensing signal, based on three independent data sets including the DLS, was remarkably lower than expected based on the Sehgal et al. (2008) X-ray based mass estimate of $M_{500}^{X\text{-}ray} = 2.2^{+0.5}_{-0.4} \times 10^{14} M_\odot$. Wittman et al. (2014) then reviewed all available mass estimates including a DLS weak lensing estimate from Sehgal et al. (2008), a dynamical estimate from Geller et al. (2010), and their own DLS weak lensing re-analysis and found that all estimates were consistent once uncertainties were properly treated. All estimates fell in the range $M_{500} = 0.8 - 2.2 \times 10^{14} M_\odot$, with the dynamical estimate at the low end and the X-ray estimate at the high end, but with no more than 2.2σ tension between them. Miyazaki et al. (2015) found a weak lensing mass favoring the low end of this range, but still with uncertainties too large to rule out the higher values. Our X-ray estimate here of $M_{500}^{X\text{-}ray} = 1.77 \pm 0.16 \times 10^{14} M_{\odot}$ reduces the statistical uncertainties and places the mass in the middle to the upper half of the range seen in the literature. We include this cluster in our mass comparison, using the weak lensing mass determined by Wittman et al. (2014).

There are outliers in the mass comparison plot of Figure 2.10, which need carry little weight in the sample mass comparison discussed below. We demonstrate this here, by addressing them individually. To start, the farthest outlier in the mass plot, marked 7b, does not have a well constrained weak lensing mass. On the other hand, its counterpart CXOU J091601 + 292750, is well supported in the X-ray as a cluster (Figure 2.4, §2.2.4), with a smooth surface distribution of photons, and a good fit to a spectrum at $z = 0.53$ with $T_X = 2.09^{+.19}_{-.19}$ keV. Its luminosity and temperature are very close to the $L_X - T_X$ relation shown in Figure 2.8. In the weak lensing analysis, this cluster is not detected significantly; it is the farthest of three clusters associated with this shear peak and was likely picked up due to the degree of smoothing of the shear field.

The second outlier in Figure 2.10, marked 2a, rests just outside the sample scatter, with a higher X-ray mass. This cluster, CXOU J052215−481816, is a bright cluster in the X-ray with robust measurements of luminosity and temperature (see Figure 2.5 for an image and spectrum). Our mass estimates depend on temperature as a proxy and are therefore subject to effects such as merger boosts. This cluster could be interacting with its neighbor, CXOU J052159−481606, which could give it a boosted temperature, and result in an artificially higher X-ray mass estimate. Simulations (Randall et al. 2002) show that mergers can affect both temperature and luminosity measurements such that this cluster may not appear as an outlier on the $L_X - T_X$

plot. And in fact, none of the clusters for which we compare masses are outliers on the $L_X - T_X$ relation in Figure 2.8 (marked with filled diamonds).

Overall Sample Comparison

The eight clusters studied here show overall agreement between the X-ray and weak lensing mass estimates, with considerable scatter. We determine a linear relationship in log-space between the masses using the methods described in Hogg et al. (2010, Eq. 35). We specifically choose this method, which allows us to estimate the intrinsic scatter of the data about the best fit relation, in order to compare to the scatter determined for other cluster samples. The relationship we fit is of the form: $\log(M_X/10^{14}M_\odot) = a + b \times \log(M_{WL}/10^{14}M_\odot)$. We convert our statistical uncertainties in mass to log-space and then symmetrize them. We report parameters obtained both with and without the two statistical outliers in the sample, clusters 2a and 7b.

The best fit relation indicates that the X-ray and weak lensing masses are consistent with one another. The slope and intercept of our best fit relation for the case where we exclude outliers are $b = 1.44^{+0.59}_{-0.41}$ and $a = -0.11^{+0.16}_{-0.23}$ which are consistent with the case of equality. Including the two outliers, the slope and intercept are $b = 1.07^{+0.73}_{-0.49}$ and $a = 0.14^{+0.18}_{-0.22}$. The intrinsic scatter of the points in the y-direction around this relation, is measured to be $47^{+42}_{-23}\%$, excluding the outliers. This scatter is plotted in Figure 2.10 (in dashed, green line). For comparison, we also plot the scatter determined from all eight points, $106^{+101}_{-43}\%$, in Figure 2.10 (in dot-dashed, blue line)[6].

We compare these results to the Canadian Cluster Comparison Project (CCCP: Mahdavi et al. 2013) who do a comparison of X-ray and weak-lensing masses using 50, massive, X-ray–selected clusters obtained from a large sky area. Selection is

[6]We also calculate scatter using the same 5 X-ray masses determined using the Arnaud et al. (2005) $M_X - T_X$ law, and find a similar scatter of 48%, which validates our earlier claim that the choice of $M_X - T_X$ law does not affect our conclusions.

the fundamental difference between the CCCP and our sample; this could result in systematic differences between the results. Weak-lensing–selection could be biased from, for example, line of sight mass projections, which could give consistently higher weak-lensing masses. The CCCP sample contains many more massive clusters than our sample, with the high end of the CCCP range being more than twice larger than our most massive cluster. Our mass range, however, excepting the lowest mass cluster, does fit comfortably within the CCCP range on its lower end. Finally, the CCCP offer multiple mass estimates from X-ray and weak lensing, and we must select values determined compatibly to ours.

Although the published mass comparison by the CCCP is for masses measured inside an overdensity radius determined through weak lensing, they offer an online tool[7] attached to a database which allows us to make a comparison more consistently with what we do. Our X-ray masses are measured within an R_{500} estimated with X-rays, and the weak–lensing masses are measured within an overdensity radius estimated from weak lensing by profile fitting, which means our two mass estimates are independent. The CCCP online tools offer access to weak–lensing masses measured within a weak lensing estimated R_{500}, and X-ray masses measured within an X-ray estimated R_{500}, which are linked to the fitting algorithm (based on Hogg et al. 2010) that they have used in their paper. We find that from all 50 X-ray–selected CCCP clusters with masses measured like ours, the CCCP sample results in an intrinsic scatter of $58\% \pm 15\%$, which is fully consistent with the intrinsic scatter of the DLS shear-selected sample (see plot of these 50 clusters with blue points in the left panel of Figure 2.11). This scatter is significantly larger than the value obtained from masses measured within identical radii: $27\% \pm 6\%$ (see plot of these with red points in the right panel of Figure 2.11); so the choice of overdensity radius is important in estimating the intrinsic scatter.

[7] http://sfstar.sfsu.edu/cccp/, (Mahdavi et al. 2013; Hoekstra et al. 2012)

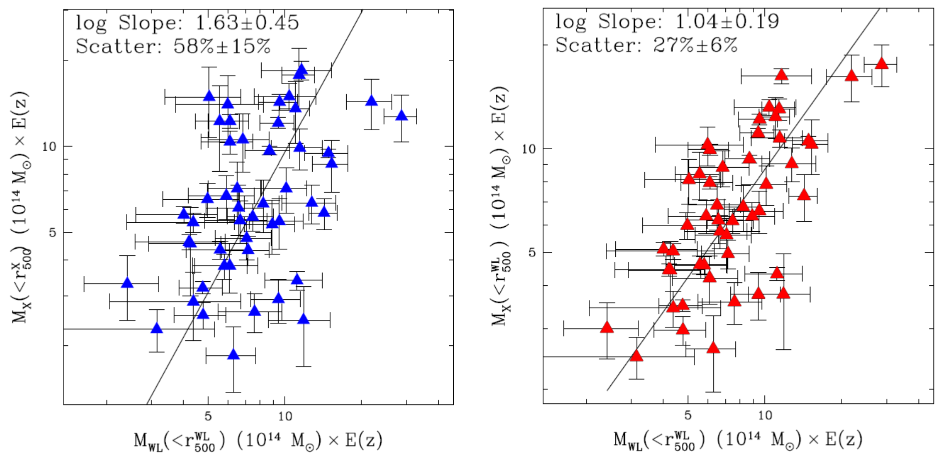

Figure 2.11 Weak lensing and X-ray mass comparison for different choices of cluster radii. On the left plot, with blue points, is the data from Mahdavi et al. (2013) and Hoekstra et al. (2012) with masses determined within differently determined radii. On the right, in the red points, are masses for the same clusters that were determined within identical radii.

The slope and intercept of our fitted mass relation is consistent with equality between X-ray and weak-lensing masses, a trait that is also exhibited by the CCCP sample (although this sample shows mild, $\sim 1\sigma$, indications of an X-ray underestimate). The large uncertainties on our scaling law relation, however, means that our mass-mass comparison is also consistent with a broad range of possible biases: for X-ray hydrostatic bias see, e.g., Vikhlinin et al. (2009), Mahdavi et al. (2013), Donahue et al. (2014), or in the context of clusters selected via the Sunyaev-Zel'dovich effect, see, e.g., von der Linden et al. (2014a), Hoekstra et al. (2015), Battaglia et al. (2015). Reducing the uncertainty on this comparison will require a much larger sample of shear-selected clusters, which will become available with future large area optical sky surveys, and targeted X-ray follow-up.

2.4 Summary

In this chapter, we present the X-ray properties and the weak lensing-to-X-ray mass comparison of the first sample of shear-selected clusters (Wittman et al. 2006). We report X-ray properties for 14 X-ray clusters that correspond to seven DLS shear peaks. An eighth DLS shear peak shows evidence for extended X-ray emission but the signal-to-noise for X-ray detection falls below our threshold for confirmation. We additionally report properties of three X-ray clusters discovered in our fields which we cannot confidently associate to shear peaks.

We determine luminosities and temperatures for 17 X-ray clusters, and also determine a luminosity-temperature relation from 13 of them with significant values of both L_X and T_X and that also correspond to the seven DLS shear peaks (Table 2.3, Figure 2.8). The clusters have widely varying X-ray properties; a factor of 6 in temperature and four orders of magnitude in luminosity. The ranges of redshift and mass of the sample are also substantial (§2.2.4). The best fit $L_X - T_X$ relation is consistent with X-ray cluster samples selected without regard for dynamical state as well as with the weak-lensing selected sample of Giles et al. (2015). Unlike this other weak-lensing study, however, we find that the DLS X-ray clusters are inconsistent with a self-similar slope for the $L_X - T_X$ relation.

We determine X-ray mass estimates using the Vikhlinin et al. (2009) X-ray mass-temperature relation. Core-excluded temperatures required for this estimate can be constrained for nine of our clusters. Weak lensing mass estimates are available for eight of them, with seven determined by A09 by fitting mass profiles centered at the X-ray peaks in *Chandra* data. An eighth weak lensing mass is available from Wittman et al. (2014) which we include in our mass comparison. We find overall agreement between the X-ray and weak lensing masses. The sample is characterized by an intrinsic scatter of $\sim 47\%$ with large uncertainty about the best fit mass relation; this is consistent with the Mahdavi et al. (2013) X-ray selected sample whose mass range largely overlaps with our sample.

We summarize some of the issues related to shear selection based on this study and other earlier work on the DLS. A major difference with other selection techniques is the association of multiple X-ray clusters with a single weak lensing shear peak — this complicates the identification of X-ray with shear. We find the shear associated X-ray clusters are not necessarily high mass individuals, and in fact, they cover an order of magnitude range in mass. Our $L_X - T_X$ relation is consistent with other X-ray cluster samples selected without regard to their dynamical activity, but is inconsistent with the self-similar relation. Weak lensing and X-ray masses determined individually for each shear–associated X-ray cluster agree broadly, and exhibit intrinsic scatter that is consistent with X-ray selected samples, as long as the two mass estimates are determined independently from one another.

Currently the number of individual, well studied, X-ray clusters from weak lensing selected samples is small, which is a consequence of the lack of large area, deep optical weak lensing surveys. As we approach the era of the Large Synoptic Survey Telescope, this issue will be alleviated.

Chapter 3

X-ray properties of SZE selected clusters from the ACT 2008 observing season.[1]

3.1 Introduction

In this chapter, I present the *XMM Newton* analysis that I contributed to the follow-up of SZE selected clusters presented in Menanteau et al. (2010b), hereafter M10b. This publication was a pioneering work. At the time, it was one of only two efforts that were confirming SZE cluster candidates from large area surveys. M10b confirmed ACT clusters from the 2008 observing season (also, Marriage et al. 2011), and Vanderlinde et al. (2010) confirmed SPT clusters; these were the first large cluster samples to come out of the two telescopes (for some early, smaller samples: Staniszewski et al. 2009; Menanteau & Hughes 2009; Hincks et al. 2010). Both of these studies used optical photometry, which is typically less expensive to obtain than other follow-up methods. The ACT follow-up campaign was designed to confirm the clusters with the confident identification of the BCG and its corresponding red sequence out to redshifts of $z \sim 0.8$. This resulted in a sample of 23 confirmed SZE selected clusters (out of 49 targets) that were published in M10b.

For this early large sample, it was important to determine the cluster properties and characterize the SZE selection. As a first step toward gaining this understanding, M10b turned to archival X-ray data from *Chandra*, *XMM Newton* and *Rosat* All Sky

[1] The work presented in this chapter is part of the publication Menanteau et al. (2010b), which is titled "The Atacama Cosmology Telescope: Physical Properties and Purity of a Galaxy Cluster Sample Selected via the Sunyaev-Zel'dovich Effect."

Survey (RASS). The archived data were used to establish X-ray flux from the ICM, as well as to determine temperatures and luminosities as indicators of cluster mass. The X-ray properties were largely used to establish whether ACT was finding the kinds of clusters that it is expected to find. Since the SZE is most sensitive to hot and massive clusters ($Y_{SZE} \sim MT_g$, §1.7.4), the (M10b) clusters should be high in mass, and would present in the X-ray as hot and luminous. M10b thus present RASS, *Chandra* and *XMM Newton* data of which I contribute the *XMM Newton* analysis.

With the *XMM Newton* data, I determine temperatures, luminosities, and fluxes anew, independently from their previous studies, so that we would have the most updated values for our clusters that were determined in a consistent way among them. We also check that the properties determined with the other telescopes are consistent with my results, in the cases when the clusters had multiple telescope observations. I discuss this analysis and the resulting properties below.

3.2 Data Analysis

XMM Newton data was available for six ACT clusters with which I determined the X-ray luminosities and temperatures. To ensure updated calibration, I ran the raw telescope data through the *XMM Newton* pipeline referencing the latest calibration files. This task and other processing tasks (e.g., spectral extraction) were conducted using the telescope proprietary analysis software, `XMM-SAS`. The resulting, newly calibrated event-lists were filtered to remove times of highly flaring background. Flaring periods were identified on light-curves, and the flare-filtered event-lists were used to generate spectra. Regions for spectral extraction were defined on pipeline processed images that we combined from the three cameras to make one soft band (0.5-2.0 keV) background-subtracted, exposure-corrected image. An initial region was chosen as a circle or an ellipse at which the emission fell below the background rate level. This

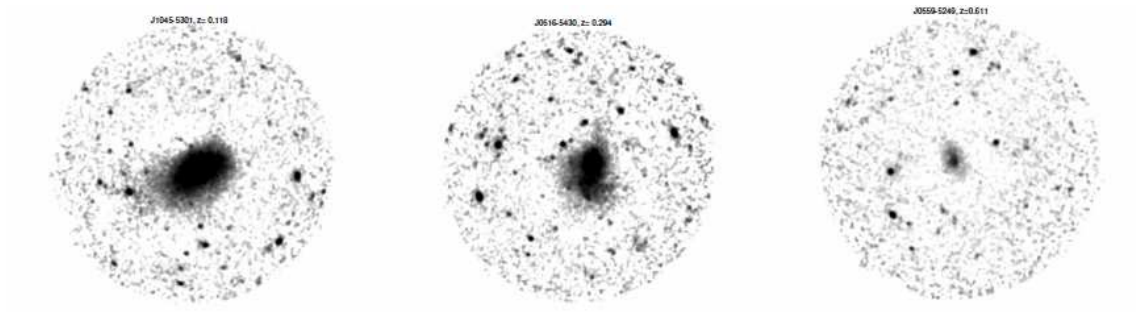

Figure 3.1 ACT clusters at low, intermediate, and high redshift going from left to right. The circular emission regions are the *XMM Newton* field of view which is centered on the cluster.

region was adjusted in 10% increments until the luminosities measured from within successive region sizes converged statistically.

To extract spectra, we filtered the event-lists further for the appropriate event patterns (patterns $\leq$ 12 for MOS, and $\leq$ 4 for PN) and to avoid events from bad chips for example. Other files necessary for spectral fitting (e.g., responses) were also generated with `XMM-SAS`, and the exposure weighting of the response function was done with the image of the cluster itself, since they produce considerable variation in brightness compared to the usually used observation exposure map. Spectra and responses were generated independently for the three cameras but were fit simultaneously to a single function in `XSPEC`. We fit to a thermal plasma (`MeKaL`) model absorbed ($\times$`phabs`) by a neutral hydrogen column density (N_H) measured by the LAB survey. Cluster redshifts were fixed, along with the N_H values, and we allowed all other parameters to vary as long as the best fit resulted in a minimum of a 3σ constraint on the parameters. When abundance could not be constrained, then we fixed it at thirty percent of the solar value ($0.3Z_{\odot}$). Luminosities and temperatures are measured using the best fit model.

Table 3.1. *XMM Newton* Cluster Properties

ACT Descriptor	z	$t_{exp}^{\rm MOS}$,$t_{exp}^{\rm PN}$ $^{(a)}$ (ks)	N_H (10^{20} cm^{-2})	$\theta_{\rm minor}$,$\theta_{\rm major}$ (arcmin)	R_{mean} $^{(b)}$ (h_{70}^{-1} kpc)	T_e (keV)	Z ($Z_\odot$)	F_X $^{(c)}$ (0.1−2.4 keV)	L_X $^{(d)}$ (0.1−2.4 keV)
ACT-CL J0145-5301	0.118	37,22	2.67	6.5,10.8	1031	5.60 ± 0.08	0.30 ± 0.02	82.96 ± 0.52	2.83 ± 0.02
ACT-CL J0645-5413	0.167	44,28	5.60	5.4,8.9	1188	7.49 ± 0.09	0.24 ± 0.01	118.70 ± 0.40	8.36 ± 0.03
ACT-CL J0516-5430	0.294	11,8	2.05	6.2,8.0	1856	7.44 ± 0.38	0.21 ± 0.05	37.57 ± 0.47	8.93 ± 0.11
ACT-CL J0658-5557	0.296	33,21	4.90	3.9,5.1	1181	10.80 ± 0.22	0.22 ± 0.03	65.22 ± 0.39	15.51 ± 0.09
ACT-CL J0330-5227	0.440	71,57	1.44	4.0,4.0	1365	5.46 ± 0.27	0.30	24.28 ± 2.34	14.60 ± 1.40
ACT-CL J0559-5249	0.611	20,14	5.06	2.0,3.5	1070	8.09 ± 0.75	0.30	5.10 ± 0.10	6.06 ± 0.12

$^{(a)}$The quoted MOS exposure time is the average of the two MOS cameras.

$^{(b)}$Geometric mean of the major and minor axes.

$^{(c)}$Units are $\times 10^{-13}$ erg s^{-1} cm^{-2}.

$^{(d)}$Units are $\times 10^{44}$ erg s^{-1}.

3.3 Results

Temperatures, luminosities, and fluxes are given in Table 3.1 and are generally consistent with fluxes from RASS and properties from *Chandra* for the overlapping cases. All clusters with *XMM Newton* or *Chandra* observations have some RASS flux, and there are three clusters in common between the *XMM Newton* and *Chandra* observations. For one ACT cluster, ACT-CL J0330-5227, the *XMM Newton* and *Chandra* flux estimates agree among themselves, but disagree with a much higher RASS flux estimate, which is likely increased due to contamination from a foreground cluster. The other two clusters, with both *XMM Newton* and *Chandra* fluxes, scatter in opposite directions of the RASS estimate, which supports the RASS value. The remaining clusters are in three way agreement.

Next I discuss the resulting luminosities and temperatures. Each cluster with an *XMM Newton* temperature has a value greater than 5 keV, the usual value for a hot cluster. This is consistent with the X-ray analysis of SPT clusters (Andersson et al. 2011), as well as with the four ACT clusters that also have *Chandra* properties in M10b. The average luminosity and temperature of clusters with *XMM Newton* properties are $\langle L_x \rangle = 9.4 \times 10^{44}$ ergs s^{-1} and $\langle kT_x \rangle = 7.5$ keV which are in good agreement with the *Chandra* results (M10b). This indeed shows, for this subset of clusters, that SZE selected clusters are hot and luminous, according to expectation, and so has laid the groundwork for more detailed X-ray follow-up (e.g., temperature or density profiles, dynamical information, masses).

I further assess how the X-ray temperatures compare to the mass thresholds estimated by M10b for their full sample ($M_{200} = 8 \times 10^{14} M_\odot$) and their high SZE signal-to-noise sample ($M_{200} = 1.0 \times 10^{15} M_\odot$). This is possible in general because mass scales with temperature (§1.8.2), which has been empirically established. I use an empirical mass-temperature relation to obtain an expected temperature for each cluster assuming a mass threshold and using the cluster redshift. The empirical relation is determined for core-excised temperatures, which can typically be higher than or comparable to temperatures measured without excising cores. And so, the core-excised temperatures estimated from the mass threshold can serve as a comparable value or a lower limit for the temperatures measured for these clusters without excising cores (Table 3.1).

I worked backwards from the two mass threshold estimates given above. First, I convert them to an overdensity radius of 500 times the critical density using a redshift averaged conversion factor of 1.8; the same as used in M10b. Then I use this mass with the mass-temperature relation of Vikhlinin et al. (2009) to estimate a temperature at each cluster's redshift. The high significance sample threshold results in core-excised temperature estimates of 8.0, 8.2, 8.8, 8.8, 9.6, and 10.6 keV, going in order from top to bottom in Table 3.1. Note that this list is also in order of increasing cluster redshift. The full sample mass threshold gives core-excised temperatures of 6.9, 7.1, 7.6, 7.6, 8.3, and 9.1 keV respectively, in the same order as above. These values suggest that up to three clusters may lie at or above the full sample threshold (ACT-CL J0645-5413, ACT-CL J0516-5430, and ACT-CL J0658-5557). Only one cluster, ACT-CL J0658-5557, which is the famous Bullet cluster, lies above the high significance threshold. From their SZE signal-to-noise, ACT-CL J0658-5557 and ACT-CL J0645-5413 are both expected to lie above the high-significance threshold value, but only one does while the other is above full sample threshold value. Additionally, again from the SZE signal-to-noise, ACT-CL J0330-5227 should also lie above the high-significance value but lies well below the full sample threshold. This cluster is discussed more in the paragraph below. There is an indication here that the temperatures are generally below the values expected from the mass thresholds, but this indication needs validation from mass and core-excised temperature measurements from the X-rays before it can cause any tension to either the estimated mass threshold or to the mass-temperature relation.

From the mass threshold estimate, it is clear that ACT-CL J0330-5227 (Abell 3128 NE) temperature is lower than expected. Although my X-ray temperature measurement of this cluster is consistent with previous work (Werner et al. 2007), a dynamical mass estimate obtained by the ACT team in Sifón et al. (2013) converted to the appropriate overdensity radius shows the mass of this cluster to be approximately $M_{500c} \sim 11 \times 10^{14} M_{\odot}$ which supports the tension associated with the x-ray temperature measurement. A recent weak lensing analysis (McCleary et al. 2015) has confirmed substructure that corresponds to infalling groups, which could be biasing the X-ray temperature measurement. A comparison of either the total mass of this cluster or its SZE signal to the gas mass could help to establish that the temperature measurement is in tension.

3.4 Discussion

The X-ray properties I determined for the subset of SZE selected clusters with *XMM Newton* observations have established the subset to be hot and luminous in accord with the expectations for SZE selection. When combined with the properties measured with *Chandra* data, then nearly half of the M10b sample is confirmed to be hot and luminous This was an important characteristic to establish for the first large set of clusters found by ACT and a first step toward assessing the SZE selection.

Some issues associated with selection and property determination arose in this work. In particular, there is good evidence that one of the temperature measurements is biased low as indicated indirectly from its high signal-to-noise SZE selection by ACT and an independent dynamical mass estimate. This cluster presents an opportunity for further study. Among other selection issues, a nice illustration of dimming in X-ray observations is given in Figure 3.1. This figure shows three comparable luminosity clusters at low, intermediate, and high redshifts, of which the lowest luminosity cluster is also at the lowest redshift. The estimation of X-ray temperatures associated with the mass threshold supported the need to determine X-ray masses for further comparison. This should prove interesting, as there are indications from *Planck* results that X-ray masses are biased low, and also that energy calibration of X-ray telescopes calibration needs further investigation (von der Linden et al. 2014a; Nevalainen et al. 2010). Overall, this work has taken the first steps to compare the ACT selection, which has since been continued (Sehgal et al. 2011; Menanteau et al. 2012; Sifón et al. 2013, 2015; Battaglia et al. 2015, are a few).

Chapter 4

Follow-up of optically selected clusters as a comparison sample for the ACT.[1]

4.1 Introduction

In this chapter, I present the X-ray analysis I contribute to Menanteau et al. (2010a). This publication was the second in a series that launched the Southern Cosmology Survey (SCS), a multi-wavelength survey in overlapping regions of the southern sky that were to be surveyed by ACT and SPT. The multi-wavelength effort aimed to uniformly generate large cluster sets from independent methods to assess the systematics of SZE selection. This second paper presented the full sample of optically selected clusters from the photometric analysis of two separate fields totaling an area of 70 deg^2.

It is useful to characterize the X-ray properties of this optical cluster sample using available data, as the X-rays help to establish an ICM and thus to identify potential sources of SZE signal for ACT and SPT surveys. In fact, two of the optical clusters presented in Menanteau et al. (2010a), hereafter SCSII were previously identified in early work by ACT or SPT (Hincks et al. 2010; Menanteau & Hughes 2009). And so, in SCSII, we present the *XMM Newton* properties for massive clusters with masses $M_{200} \geq 3 \times 10^{14} M_{\odot}$ which is a safe lower limit for SZE. It is now well-known that for flux or exposure limited surveys, there are more optical counterparts to X-ray

[1]The analysis I present in this chapter is published in Menanteau et al. (2010a) as part of a larger effort.

clusters, than there are X-ray counterparts to optical clusters (Donahue et al. 2001, 2002). Confirming X-ray emission from the optically selected sample is thus important to establishing a useful comparison sample to SZE selected clusters.

In general, optical (photometric) selection has the advantage of being relatively inexpensive (when compared to other selection methods) and can be sensitive to much smaller cluster masses than other techniques. The big disadvantage however is obtaining reliable masses as this method has historically been subject to severe contamination from projection effects. A secondary goal of the X-ray follow-up presented here then is to further confirm the optical masses, as the mass is the effective quantity on which the SZE selects clusters.

4.2 *XMM Newton* follow-up

XMM Newton observations were available in parts of both of the optical fields, the 5-hour field, and the 23-hour field, named after the hour-angles of their central coordinates; however the overlap was over less than 50% of their areas. These X-ray observations were being collected as part of the Blanco Cosmology Survey (BCS) (Šuhada et al. 2012) and all had exposures in the range of $10 - 20$ ks. In particular there were five observations that coincided with the SCSII clusters: obsIDs 0205330301, 0505380601, 0505381801, 0505382201, and 0505383601. The analysis of these observations is largely in line with the *XMM Newton* analyses described elsewhere in this thesis, and so I give only the highlights below.

Source identification

We construct images for viewing sources and to identify regions in the $(0.5 - 2.0$ keV$)$ band by co-adding the images provided by the telescope pipeline *XMM-PPS* (PPS) for a given observation. We use these first to confirm by eye the extended sources identified in the PPS wavelet-based source detection. We list PPS sources that are within 30″ of an SCSII cluster in Table 4.1 along with their *XMM Newton* IDs, offsets from the optical positions, and whether or not they were flagged as extended by the PPS. For the SCS sources that did not have corresponding PPS X-ray detections, we determine X-ray properties from nominal regions to asses flux (and mass) limits.

Determining X-ray properties

Fluxes and luminosities were extracted from within circular regions placed around the *XMM Newton* positions (or the SCS ones when there was no nearby PPS source). For the extended sources, regions were ensured to contain all of the cluster emission by an iterative process that involved increasing the radius in steps to achieve the maximal count rate at the best signal-to-noise ratio. For other sources, regions were fixed to be 1′ in size and centered on the SCS coordinate (excepting the non-extended PPS source whose region was centered on the XMM coordinate). The background was estimated from annular circular regions that were large enough to ensure good photon statistics; these were placed to surround the source while avoiding any source emission and also had PPS point sources excluded from them. Count rates from within these are quoted in Table 4.1.

We extracted products from the spectral analysis ourselves using the telescope analysis software (`XMM-SAS`). Spectra, and other files (arfs and rmfs) were extracted from PPS event-lists that we filtered to remove background flares. Luminosities and fluxes in the 0.5–2.0 keV band were extracted from the best fitting spectral model that describes a thermal plasma with line emission.

We fit the spectra in `XSPEC` to the `MeKaL` model which was multiplied additionally by an absorbing component (`phabs`). The neutral hydrogen column density for the absorbing component was fixed to the values measured by the LAB survey. Values of solar abundance were fixed to be 0.3 times the solar value in the `MeKaL`

Table 4.1. Optical Clusters Located within the Field of View of XMM-Newton Observations

SCS ID	$z_{\rm cluster}$	$N_{\rm H}$ (10^{20} cm^{-2})	X-ray ID	Offset ($''$)	Extended?	Extr Rad (kpc)	Rate (0.5–2 keV) (10^{-3}cts s^{-1})	L_X (0.5–2.0 keV) (10^{44} ergs s^{-1})	$M(L_X)$ (10^{14} $M_\odot$)
SCSO J051558−543906	0.64	2.07	XMM J051600−543900	19	yes	910 (2.2$'$)	15.7 ± 2.6	0.60	3.0
SCSO J051613−542620	0.36	1.98	...	...	...	300 (1$'$)	6.8 ± 1.4	0.027	0.5
SCSO J051637−543001	0.2952*	2.05	XMM J051635−543022	25	yes	1390 (5.3$'$)	1740 ± 15	5.1	14.4
SCSO J231651−545356	0.36	1.29	XMM J231653−545410	26	yes	650 (2.2$'$)	73.7 ± 3.5	0.71	4.1
SCSO J232856−552428	0.57	1.29	XMM J232856−552429	5	no	390 (1$'$)	5.4 ± 1.3	0.07	0.8
SCSO J233420−542732	0.55	1.27	...	...	...	380 (1$'$)	5.2 ± 1.4	0.08	0.9
SCSO J233556−560602	0.63	1.27	...	...	...	410 (1$'$)	6.2 ± 1.7	0.10	1.0

Note. — Luminosities calculated by fitting an absorbed thermal emission model with a fixed 5 keV temperature, except for SCSO J051558−543906, SCSO J051637−543001, and SCSO J231651−545356 for which there was enough signal to determine their temperatures (see text). The quoted redshifts are just repeated from Tables 3 and 4 of SCSII except for the starred value which is a spectroscopic redshift from NED (see Table 5, SCSII).

model. Additionally the redshift values were fixed to those in SCSII, except for SCSO J051637-543001 for which we use the spectroscopic value listed in NED. The resulting luminosities and fluxes are given in Table 4.1 for both the extended and non-extended PPS sources, as well as for the SCS source for which there was no nearby significant X-ray source.

We estimate X-ray masses from the luminosities using an empirically determined luminosity-mass scaling relation (Vikhlinin et al. 2009). These masses are measured within an overdensity radius equal to $\Delta = 500$ times the critical density $\rho_c = 3H^2/8\pi G$, which we transform to an estimate inside an overdensity radius corresponding to $\Delta = 200$ times ρ_c overdensity radius with a multiplicative factor of 1.77, which is reasonable to 10% for the redshift and mass ranges of these clusters.

Resulting X-ray properties

Of the seven SCS clusters observed by *XMM Newton*, three have sufficient signal for the spectral fits to constrain a temperature alongside the luminosity. SCSO J051558-543906 and SCSO J231651-545356 fit to temperatures of $kT = 1.8^{+0.5}_{-0.3}$ keV and $kT = 3.7^{+0.6}_{-0.5}$ keV respectively. The third SCS source, SCSO J231651-545356, is a bright Abell cluster (Abell S0520). We find the temperature and abundance of this cluster to be $kT = 7.7 \pm 0.3$ keV and 0.17 ± 0.04 relative to solar, both of which are consistent with earlier work (Zhang et al. 2006).

For the remaining SCS sources, we assume and fix a temperature of 5 keV in the spectral fits and report the resulting luminosities. These four sources are detected significantly as indicated by their photon count rates, but have a median luminosity that is an order of magnitude lower compared to the other clusters.

The X-ray masses agree well with the optical masses estimated from member counts for the three clusters with X-ray temperature measurements. For three more

SCS clusters, X-ray masses lie below the optical ones by factors of 3—5. This discrepancy could improve with deeper X-ray follow-up to obtain more accurate values of the luminosity (and also constrain at least a temperature). The final cluster, SCSO J051613-542620, has an order of magnitude discrepancy between the masses, which is likely due to contamination in the optical galaxy membership by the nearby rich cluster Abell S0520. These systems are also close in redshift (0.36 and 0.2952).

The masses estimated from *XMM Newton* here, were included in a broader comparison in SCSII between X-ray and optical derived masses for the full optical sample. This showed that X-ray and optical masses can easily differ by a factor of two, and furthermore (through a stacking analysis) that the discrepancy tends to be worse for high redshift and high (optical) mass clusters (Menanteau et al. 2010a).

4.3 Discussion

X-ray analysis of the subset of optically selected clusters shown here have confirmed that some of the clusters are indeed massive enough to be seen by ACT (namely, SCSO J051637–543001 is seen by both ACT and SPT as ACT-CL J0516–5432 and SPT-CL 051–5430). The remaining clusters have low-significance measurements of X-ray flux, although their count rates are significant. This suggests that deeper X-ray observations to properly constrain temperatures, luminosities and masses. Part of the reason for this is that many of them are intermediate to high redshift systems. This is a typical selection issue seen in optical and X-ray selection comparisons. The need for deeper data here is consistent with that described by Šuhada et al. (2012) from their analysis of six square degrees of ~ 10 ks *XMM Newton* observations, some of which overlap with our sample.

There may be an additional selection issue in play here. The optical masses here are calibrated with weak lensing masses (Reyes et al. 2008), and so their comparison to

X-ray masses can be subject to known issues in weak lensing to X-ray comparison. In particular, line of sight extensions of triaxial halos or filaments may be contributing to the discrepancy between the X-ray fluxes observed here and the weak lensing calibrated optical masses. If this is the case, then it may also be influencing the calibrations with optical luminosity versus richness differently; an element of support for this difference is that none of the clusters with low-significance X-ray flux have agreeing mass estimates between their optical luminosity derived mass and optical richness derived mass. Confirmation of this would also require better understanding of the X-ray properties of the clusters (e.g., Giles et al. 2015) which would be obtained through deeper X-ray observations.

Conclusion and Future Work

X-ray analyses presented here inform the selection and mass-determination of clusters discovered in surveys that were selected on mass or were approximately mass limited. In chapter two, I present the properties of a unique set of clusters, selected primarily by their shear signal-to-noise. The masses I determine for them indicate that the shear on which they were selected is likely the summed result of multiple contributing clusters (identified in previous work). The multiple cluster selection is attributed to heavy smoothing in the shear maps, the usefulness of which can now be better considered. On the one hand, clusters such as Abell 781 "west", DLSCL J0522.2-4820 "C" (W06, nomenclature) or DLSCL J0916.0+2931 "7b" (A09, nomenclature) would not necessarily have been found on their shear alone, which is below a detection significance of 3σ in some analyses. On the other hand, the cluster properties of the sample do not lend themselves to clean characterizations for modeling of selection effects (e.g., Malmquist bias is an effect that *can* be modeled and corrected for). Drawing a mass function of clusters selected in highly smoothed shear from a much larger set would be useful to determine if this selection can provide a complete cluster sample (within some redshift window) down to a mass threshold, or if it introduces new selection effects. These questions about weak lensing selection can be tackled by the ongoing Dark Energy Survey (DES Vikram et al. 2015) and upcoming LSST.

The mass comparison I have presented in Chapter two for the shear selected sample is consistent with that of the much larger sample of X-ray selected clusters in the CCCP. Both of these studies have indicated that X-ray and weak lensing masses are consistent with each other but with large scatter; this scatter is larger than both the line of sight uncertainty in weak lensing mass estimation as well as the expected bias in hydrostatic X-ray mass estimation combined. Beating down this scatter is important to improve the usefulness of weak lensing in the efforts to calibrate masses estimated with other methods. It may not be a matter of acquiring larger comparison data sets alone since the CCCP finds the same large scatter for 50 clusters, but rather the matter of making more careful characterizations with better data (or instruments). An alternative direction of investigation may be to see if there is a third fundamentally linked quantity with which to draw a three-way relationship that would more tightly relate the X-ray and weak lensing information. Such a quantity could be some measure of dynamical activity which would affect the X-ray measurement, or alternatively, an indicator of halo shape or a measure of substructure which could affect both. Reformulating the comparison to be between masses measured within the same radii (as estimated from either X-ray or weak lensing) has already been shown to result in a much lower scatter comparison (e.g., Mahdavi et al. 2013). Returning to the idea of carefully using better data, recent efforts with the Dark Energy Camera (DECam) have improved the depth of weak lensing analysis and with this shown that it is possible to constrain the masses of infalling group sized halos (at low redshift McCleary et al. 2015), emphasizing that the sum of substructure is better constrained than its components. We find also, considering the masses of the Abell 781 components, that the summed X-ray and the summed weak lensing masses are in better agreement. This agreement may have fundamental implications to better understanding the scatter in weak lensing estimation. Giles et al. (2015) have also presented evidence that shear selected (isolated) clusters are under-luminous in the X-rays owing to either elongated line of sight orientations or filaments. For weak lensing and X-ray comparison studies, we are still in the regime in which detailed, careful characterizations of modest-sized samples help to build reliable relationships that may be applied to larger data sets. There is still more survey area within the

DLS and completing its X-ray follow-up would be a first step along with obtaining even deeper X-ray observations of the same cluster sample presented in Chapter two, so that masses could be measured for the more distant clusters. The X-ray follow-up of the entire 20 deg^2 DLS has comparison samples from optical analysis ready to go (Ascaso et al. 2014) and could be additionally compared with the *Planck* all sky survey for comparison to SZE selection.

In Chapters three and four, I used X-ray data to assess the expectations for SZE selected clusters, both in preparation for and following the pioneering discovery of the first large set of SZE selected clusters from ACT.

In Chapter four, I determined the X-ray temperatures, luminosities and masses for a subset of clusters which helped to establish that the optically selected clusters would indeed be a good high mass comparison set for ACT to compare selection with. Known issues between optical and X-ray selection surfaced (e.g., that there are fewer clusters with X-ray emission, consistently with previous work: Donahue et al. 2001) and limited the scope of the work by reducing the number of clusters with significant X-ray properties. Still, the resulting information was in accord with the optical estimates, confirming that the clusters with significant X-ray properties were indeed good (massive) candidates that would be seen by ACT.

As it has turned out, as shown with an estimate from cluster counts by M10b, the ACT mass threshold for this early sample is around $M_{200} = 8 \times 10^{14} M_{\odot}$, and not the lower value of $3 \times 10^{14} M_{\odot}$ with which the SCSII sample was generated. Consequently, there is only one cluster in the entire 70 deg^2, with X-ray properties and a sufficiently high mass to have been seen by ACT. The clusters without X-ray counterparts seem to have been selected due to either one or the other of their N_{200} and L_{200} based mass estimates (the other lying below the threshold). For the high mass subset with X-ray observations, there is an indication that the lack of X-ray emission from some clusters may have more to do with their selection in the optical than the previously referenced

X-ray versus optical selection issues. And so in this work, the X-ray follow-up has helped to definitively identify clusters visible to ACT, modulo the ACT detection threshold.

In Chapter three, I describe my work involved in establishing X-ray emission and determining cluster properties for a subset of the first large sample of SZE selected clusters from ACT. Overall, the subset of clusters I characterized is consistent with the expected sensitivity of SZE selection to high masses. One of the clusters I analyzed, ACT-CL J0330-5227, has been shown to have infalling substructure which challenges the usual assumptions for relating properties to mass, and at least in this case, is likely biasing the X-ray properties. This would make an interesting case for further study because although it is known that dynamical interaction influences the temperature measurement, the amount of influence on the temperature is high for this cluster. As for the mass-temperature relation that sets its temperature expectation, there is evidence for the lack of significant influence on scaling laws derived including disturbed systems (Sifón et al. 2013). Another interesting task would be to compare the SZE signal or mass estimate to a measurement of its gas mass. The next step for this sample would be to determine X-ray masses for comparison, as well as X-ray estimates of other proxies (gas mass, and thermal energy).

The efforts described in this thesis contribute to building large well characterized sets of clusters to assess their multi-wavelength selection and mass determination. Upcoming and ongoing large area surveys and follow-up efforts are expected to include hundreds of clusters. Large numbers are necessary to investigate the scatter in scaling laws, and typically smaller samples identify the areas of investigation. The samples studied here have shown that careful studies are necessary to build more reliable relationships between observational parameters. The need for deep X-ray observations in particular is a strong one for establishing reliable characterizations and understanding sources of systematic scatter. The possibility of SZE surveys to provide rare high-redshift, high-mass clusters that provide strong constraints on cosmology has now been demonstrated (Sehgal et al. 2011; Hasselfield et al. 2013). By applying a fiduciary scaling relation between SZE signal and the cluster mass to nine high SZE signal clusters, Sehgal et al. (2011) find that clusters alone can constrain σ_8 and w to better accuracy than from the CMB alone. However, variations to the fiduciary scaling relations arise from non-gravitational and non-thermal physical processes that also represent the limits of our understanding or our ability to accurately model the gas physics. When parameters of the scaling relation are allowed to vary in accord with influences of non-thermal and non-gravitational processes, both studies above show that constraints from the SZE selected clusters get washed out. Hasselfield et al. (2013) identify some dependencies of the relation on such processes and the consequential influences to cosmological parameter estimation. More detailed and accurate measurements of observables associated with the gas (or also other cluster components) will help to characterize the systematic variations in the scaling relations and so then to draw tighter relationships between the observables and cluster mass. And so, there is a still persisting need to carry out deeper studies of cluster properties, like the study described in chapter two, or others referenced throughout this thesis. More cluster samples with deeper observations or larger numbers of clusters that are becoming available now and in the near future will help to achieve the better understanding of clusters and scaling relations necessary to provide stronger constraints on cosmology and also to probe cosmology more accurately at other spatial scales and energy scales.

Bibliography

Abadi, M. G., Moore, B., & Bower, R. G. 1999, MNRAS, 308, 947

Abate, A., Wittman, D., Margoniner, V. E., et al. 2009, ApJ, 702, 603

Akritas, M. G., & Bershady, M. A. 1996, ApJ, 470, 706

Allen, S. W., Rapetti, D. A., Schmidt, R. W., et al. 2008, MNRAS, 383, 879

Allen, S. W., Schmidt, R. W., & Fabian, A. C. 2001, MNRAS, 328, L37

Andersson, K., Benson, B. A., Ade, P. A. R., et al. 2011, ApJ, 738, 48

Arnaud, M., & Evrard, A. E. 1999, MNRAS, 305, 631

Arnaud, M., Pointecouteau, E., & Pratt, G. W. 2005, A&A, 441, 893

Ascaso, B., Wittman, D., & Dawson, W. 2014, MNRAS, 439, 1980

Bahcall, N. A., & Fan, X. 1998, ApJ, 504, 1

Battaglia, N., Leauthaud, A., Miyatake, H., et al. 2015, ArXiv e-prints, arXiv:1509.08930

Becker, M. R., & Kravtsov, A. V. 2011, ApJ, 740, 25

Budavári, T., Szalay, A. S., Connolly, A. J., Csabai, I., & Dickinson, M. 2000, AJ, 120, 1588

Butcher, H., & Oemler, Jr., A. 1984, ApJ, 285, 426

Carlstrom, J. E., Holder, G. P., & Reese, E. D. 2002, ARA&A, 40, 643

Cook, R. I., & Dell'Antonio, I. P. 2012, ApJ, 750, 153

Dawson, K. S., Schlegel, D. J., Ahn, C. P., et al. 2013, AJ, 145, 10

Dodelson, S. 2003, Modern cosmology

Donahue, M., Mack, J., Scharf, C., et al. 2001, ApJL, 552, L93

Donahue, M., Scharf, C. A., Mack, J., et al. 2002, ApJ, 569, 689

Donahue, M., Voit, G. M., Mahdavi, A., et al. 2014, ApJ, 794, 136

Dressler, A. 1984, ARA&A, 22, 185

Duffy, A. R., Schaye, J., Kay, S. T., & Dalla Vecchia, C. 2008, MNRAS, 390, L64

Ettori, S. 2013, MNRAS, 435, 1265

Fowler, J. W., Acquaviva, V., Ade, P. A. R., et al. 2010, ApJ, 722, 1148

Gavazzi, R., & Soucail, G. 2007, A&A, 462, 459

Geller, M. J., Hwang, H. S., Fabricant, D. G., et al. 2014, ApJS, 213, 35

Geller, M. J., Kurtz, M. J., Dell'Antonio, I. P., Ramella, M., & Fabricant, D. G. 2010, ApJ, 709, 832

Giles, P. A., Maughan, B. J., Hamana, T., et al. 2015, MNRAS, 447, 3044

Gladders, M. D., & Yee, H. K. C. 2001, in Astronomical Society of the Pacific Conference Series, Vol. 232, The New Era of Wide Field Astronomy, ed. R. Clowes, A. Adamson, & G. Bromage, 126

Hasselfield, M., Hilton, M., Marriage, T. A., et al. 2013, JCAP, 7, 008

Hilton, M., Romer, A. K., Kay, S. T., et al. 2012, MNRAS, 424, 2086

Hincks, A. D., Acquaviva, V., Ade, P. A. R., et al. 2010, ApJS, 191, 423

Hoekstra, H., Herbonnet, R., Muzzin, A., et al. 2015, MNRAS, 449, 685

Hoekstra, H., Mahdavi, A., Babul, A., & Bildfell, C. 2012, MNRAS, 427, 1298

Hogg, D. W., Bovy, J., & Lang, D. 2010, ArXiv e-prints, arXiv:1008.4686

Hubble, E. 1929, Proceedings of the National Academy of Science, 15, 168

Kaastra, J. S. 1992, An X-Ray Spectral Code for Optically Thin Plasmas, Internal SRON-Leiden Report, updated version 2.0

Kaiser, N. 1986, MNRAS, 222, 323

—. 1992, ApJ, 388, 272

Kalberla, P. M. W., Burton, W. B., Hartmann, D., et al. 2005, A&A, 440, 775

Koester, B. P., McKay, T. A., Annis, J., et al. 2007, ApJ, 660, 239

Kravtsov, A. V., Vikhlinin, A., & Nagai, D. 2006, ApJ, 650, 128

Kubo, J. M., Khiabanian, H., Dell'Antonio, I. P., Wittman, D., & Tyson, J. A. 2009, ApJ, 702, 980

Mahdavi, A., Hoekstra, H., Babul, A., et al. 2013, ApJ, 767, 116

Mantz, A., Allen, S. W., & Rapetti, D. 2010, MNRAS, 406, 1805

Markevitch, M. 1998, ApJ, 504, 27

Marriage, T. A., Baptiste Juin, J., Lin, Y.-T., et al. 2011, ApJ, 731, 100

Maughan, B. J., Giles, P. A., Randall, S. W., Jones, C., & Forman, W. R. 2012, MNRAS, 421, 1583

McCleary, J., dell'Antonio, I., & Huwe, P. 2015, ApJ, 805, 40

Mellier, Y. 1999, ARA&A, 37, 127

Menanteau, F., & Hughes, J. P. 2009, ApJL, 694, L136

Menanteau, F., Hughes, J. P., Barrientos, L. F., et al. 2010a, ApJS, 191, 340

Menanteau, F., González, J., Juin, J.-B., et al. 2010b, ApJ, 723, 1523

Menanteau, F., Hughes, J. P., Sifón, C., et al. 2012, ApJ, 748, 7

Menanteau, F., Sifón, C., Barrientos, L. F., et al. 2013, ApJ, 765, 67

Mewe, R., Gronenschild, E. H. B. M., & van den Oord, G. H. J. 1985, A&AS, 62, 197

Mewe, R., Lemen, J. R., & van den Oord, G. H. J. 1986, A&AS, 65, 511

Miyazaki, S., Hamana, T., Ellis, R. S., et al. 2007, ApJ, 669, 714

Miyazaki, S., Oguri, M., Hamana, T., et al. 2015, ApJ, 807, 22

Mushotzky, R. F., Serlemitsos, P. J., Boldt, E. A., Holt, S. S., & Smith, B. W. 1978, ApJ, 225, 21

Navarro, J. F., Frenk, C. S., & White, S. D. M. 1997, ApJ, 490, 493

Nevalainen, J., David, L., & Guainazzi, M. 2010, A&A, 523, A22

Oke, J. B., Cohen, J. G., Carr, M., et al. 1995, PASP, 107, 375

Planck Collaboration, Ade, P. A. R., Aghanim, N., et al. 2015, ArXiv e-prints, arXiv:1502.01589

Pratt, G. W., Croston, J. H., Arnaud, M., & Böhringer, H. 2009, A&A, 498, 361

Press, W. H., & Schechter, P. 1974, ApJ, 187, 425

Randall, S. W., Sarazin, C. L., & Ricker, P. M. 2002, ApJ, 577, 579

Reyes, R., Mandelbaum, R., Hirata, C., Bahcall, N., & Seljak, U. 2008, MNRAS, 390, 1157

Riess, A. G., Press, W. H., & Kirshner, R. P. 1996, ApJ, 473, 88

Ruhl, J., Ade, P. A. R., Carlstrom, J. E., et al. 2004, in Proc. SPIE, Vol. 5498, Z-Spec: a broadband millimeter-wave grating spectrometer: design, construction, and first cryogenic measurements, ed. C. M. Bradford, P. A. R. Ade, J. E. Aguirre, J. J. Bock, M. Dragovan, L. Duband, L. Earle, J. Glenn, H. Matsuhara, B. J. Naylor, H. T. Nguyen, M. Yun, & J. Zmuidzinas, 11–29

Sarazin, C. L. 1988, X-ray emission from clusters of galaxies

Schirmer, M., Erben, T., Hetterscheidt, M., & Schneider, P. 2007, A&A, 462, 875

Sehgal, N., Hughes, J. P., Wittman, D., et al. 2008, ApJ, 673, 163

Sehgal, N., Trac, H., Acquaviva, V., et al. 2011, ApJ, 732, 44

Sifón, C., Menanteau, F., Hasselfield, M., et al. 2013, ApJ, 772, 25

Sifón, C., Battaglia, N., Menanteau, F., et al. 2015, ArXiv e-prints, arXiv:1512.00910

Staniszewski, Z., Ade, P. A. R., Aird, K. A., et al. 2009, ApJ, 701, 32

Starikova, S., Jones, C., Forman, W. R., et al. 2014, ApJ, 786, 125

Sun, M., Voit, G. M., Donahue, M., et al. 2009, ApJ, 693, 1142

Sunyaev, R. A., & Zeldovich, Y. B. 1970, Comments on Astrophysics and Space Physics, 2, 66

—. 1972, Comments on Astrophysics and Space Physics, 4, 173

Tyson, J. A., Valdes, F., & Wenk, R. A. 1990, ApJL, 349, L1

Utsumi, Y., Miyazaki, S., Geller, M. J., et al. 2014, ApJ, 786, 93

Šuhada, R., Song, J., Böhringer, H., et al. 2012, A&A, 537, A39

Vanderlinde, K., Crawford, T. M., de Haan, T., et al. 2010, ApJ, 722, 1180

Vikhlinin, A., Burenin, R. A., Ebeling, H., et al. 2009, ApJ, 692, 1033

Vikram, V., Chang, C., Jain, B., et al. 2015, Phys. Rev. D, 92, 022006

von der Linden, A., Mantz, A., Allen, S. W., et al. 2014a, MNRAS, 443, 1973

von der Linden, A., Allen, M. T., Applegate, D. E., et al. 2014b, MNRAS, 439, 2

Weinberg, N. N., & Kamionkowski, M. 2003, MNRAS, 341, 251

Werner, N., Churazov, E., Finoguenov, A., et al. 2007, A&A, 474, 707

Wittman, D., Dawson, W., & Benson, B. 2014, MNRAS, 437, 3578

Wittman, D., Dell'Antonio, I. P., Hughes, J. P., et al. 2006, ApJ, 643, 128

Wittman, D. M., Tyson, J. A., Dell'Antonio, I. P., et al. 2002, in Proc. SPIE, Vol. 4836, Survey and Other Telescope Technologies and Discoveries, ed. J. A. Tyson & S. Wolff, 73–82

Wright, E. L. 2006, PASP, 118, 1711

Zhang, Y.-Y., Böhringer, H., Finoguenov, A., et al. 2006, A&A, 456, 55

Zwicky, F. 1933, Helvetica Physica Acta, 6, 110

—. 1937, ApJ, 86, 217